Towards Pulsed Telecom Laser Ablation Loading for an Ytterbium Ion Trap

by

Jingwen (Monica) Zhu

A thesis
presented to the University of Waterloo
in fulfillment of the
thesis requirement for the degree of
Master of Science
in
Physics (Quantum Information)

Waterloo, Ontario, Canada, 2023

Author's Declaration

I hereby declare that I am the sole author of this thesis. This is a true copy of the thesis, including any required final revisions, as accepted by my examiners.

I understand that my thesis may be made electronically available to the public.

Abstract

Trapped ion system is a promising platform for quantum computing, with long qubit coherence, high gate and measurement fidelities. To harness the full potential of the trapped ion system, it is imperative to employ an efficient ion loading scheme. While the conventional oven loading method has its drawbacks, such as slow loading time, resource wastage, and potential contamination that can compromise system longevity and introduce decoherence, the pulsed laser ablation loading offers a promising alternative. This method enables fast, resource efficient, and controllable generation of a neutral atomic flux.

This thesis explores the development of a 1.57 μm pulsed laser ablation (PLA) loading scheme for an Ytterbium ion trap. With endeavors in theoretical simulations and experimental setups designed with a keen emphasis on laser-induced damage thresholds, we successfully generated a neutral flux from the ablation laser, acquired a comprehensive isotope spectrum, and estimated the velocity distribution in the atomic plume. A fiber-coupled ablation delivery module was also designed and proved feasible along with the main ablation experiments.

This study establishes a solid groundwork for the future integration of pulsed laser ablation loading into our trap system and provides invaluable empirical insights into the use of high-power infrared (IR) pulsed lasers.

Acknowledgements

I am deeply thankful to my supervisor, Prof. Kazi Rajibul Islam, for giving me invaluable guidance on the thesis. His patience and trust have given me the space to make mistakes, learn, and grow. I'm greatly grateful to my committee members, Prof. Joe Sanderson and Prof. Jim Martin, for joining my advisory committee and dedicating precious time on thesis review.

I sincerely appreciate all members of the QITI lab for fostering a caring and creative environment. I enjoy discovering sparkling talents of my fellow labmates: Yu-Ting, Sainath, Gilbert, Nikhil, Lewis, Anthony, Sakshee, as well as the many co-op students I've had the chance to work with.

I want to thank friends from other labs: Brendan, Pei-Jiang, Noah, Collin, Akbar, Hawking, and members from Jungsang Kim's group at Duke University. Their suggestions and insights have helped me avoid many obstacles along the way.

The last thank-you is reserved for my mother F.H., my boyfriend X.X., my dearest chihuahuas Jupiter and Mars. Their unwavering companion and unconditional love are the roots of my strength and confidence, propelling me forward through challenging times and keeping me trying to be a better self.

Dedication

This is dedicated to the nature and the ones I love.

Table of Contents

List of Figures

List of Tables

Chapter 0

Introduction

The trapped ion system is a promising quantum computing platform that utilizes internal atomic energy levels to store quantum information.[2, 3] Thanks to the long lifetime of the commonly chosen energy states and improving optics shaping, addressing and imaging techniques, trapped ions as qubits stand out for their long coherence time and high gate and measurement fidelities.

The workflow of using a trapped ion quantum computer consists of ion loading, qubit state initialization, gates or evolution, and qubit state measurement. To enjoy the benefits of a trapped ion system, one must start with a good ion loading scheme that is fast and resource efficient. The general loading procedure is to first generate a neutral atomic vapor, then ionize the neutral atoms at the desired trapping region. See Sec.1.2.2 for a detailed example of loading Yb ions. Resistively heated oven was our first choice to generate the atomic vapor as a conventionally popular and easily implementable method. However, ovens typically take minutes to warm up and cool down, resulting in atom wastage and delaying experiment. We turned to exploring pulsed laser ablation (PLA) loading for a fast, economical, and controllable loading approach. Chap.1 offers a detailed explanation of the motivation behind PLA loading, contrasting it with the oven method.

This thesis project was initiated as a first step to develop a PLA loading scheme using a 1.57 μm pulsed laser for an Ytterbium ion trap in Quantum Information with Trapped Ions (QITI) Lab. On the theoretical front, we have built simulation tools to better understand and study the dynamics of the plume, as detailed in Chap.2. Experimentally, my main focus was on designing and setting up the optics with strong attention to laser safety, discussed in Chap.3. Combining all these efforts, we were able to generate a neutral atomic flux from the ablation laser, gather an isotope spectrum, and estimate the velocity spread in

the atomic plume. The experimental findings and their analysis are presented in Chap.4.

0.1 Thesis Outline and Author's Contribution

The thesis is organized as follows, highlighting the author's contributions:

- Chapter.1 begins with a concise overview of the trapped ion quantum computing system, emphasizing the advantages of PLA loading over traditional ovens. It then introduces Ytterbium ions as hyperfine ion qubits and delves into the a specific 2-step ionization loading scheme to achieve isotope selectivity. The chapter concludes by discussing the broadening effects of the neutral detection transition (399 nm line) to set the stage for the simulation in the subsequent chapter.

- Chapter.2 delves into the Monte Carlo simulation of the expected single atom fluorescence and a full spectrum of the 399 nm transition under various plume conditions. The simulation algorithm was designed and implemented by the author.

- Chapter.3 provides a detailed guide to the optics setup, emphasizing the laser-induced damage thresholds. It also presents other equipment like the chamber, vacuum, and metal target. Additionally, a fiber-coupled ablation beam delivery plan is discussed alongside as a feasibility test. The author is credited for designing and setting up all the optics and hardware. Acknowledgements are given for invaluable support from Collin Epstein, Lewis Hahn, Chung-you Shih on the electronic control system (ARTIQ), and to Sainath Motlakunta, Nikhil Kotibhaskar, and former colleagues for the chamber and ablation target holders design and fabrication.

- Chapter.4 offers preliminary results and insights obtained from the existing setup. Experiments included fluorescence signal versus ablation fluencef and the lifetime of the ablation spot. The author was responsible for both the experimental design and analysis. Gratitude is extended for meaningful discussions with Pei Jiang Low, Brendan White, Noah Greenberg and members of Prof. Jungsang Kim's group from Duke University.

- Chapter.5 reviews the project's progress and anticipates future experiments made possible by the current setup. The author outlines the forthcoming steps and potential enhancements to the existing setup.

Chapter 1

Background

Firstly, in Sec.1.1, I will provide motivation for using pulsed laser ablation (PLA) loading by briefly explaining the loading process and comparing the conventional oven loading with PLA loading. Secondly, in Sec.1.2, I explain the process of loading ytterbium ions using a two-step ionization scheme, to familiarize readers with the involved transitions. Lastly, in Sec.1.3, I delve into transition broadening effects, specifically power broadening and Doppler broadening, which are taken into account in the simulations presented in the subsequent chapter.

1.1 Ion Trap Fundamentals

Ion Trapping To confine ion movements, one aims to create an effective potential of the form

$$V = ax^2 + by^2 + cz^2 \quad \text{where } a, b, c > 0 \tag{1.1}$$

for confinement in all three dimensions. However, as described by Earnshaw's theorem, this potential cannot be achieved in free space with static electric field only because following Maxwell's equations

$$\nabla^2 V = 0 \Rightarrow a + b + c = 0 \tag{1.2}$$

i.e. at least one factor is negative thus anti-confining in the corresponding dimension. A widely used technique, introduced by Wolfgang Paul [4], uses oscillating spatially inhomogeneous electric field generated by radio frequency (RF) quadrupoles in addition to the

static field to create a pondermotive potential that resembles the form of the aforementioned three-dimensional harmonic potential well,

$$V_{pond} = \frac{1}{2m}(\omega_x^2 x^2 + \omega_y^2 y^2 + \omega_z^2 z^2) \tag{1.3}$$

The movement of ions at the pondermotive frequencies is called secular motion. The ions also perform micromotion at the same frequency as the oscillating RF field. Ideally, the ion's equilibrium position is placed at the RF null, where the RF field strength is zero, so that micromotion is minimized. However, due to displacement by static electric field mismatch, ion may be placed away from the RF null seeing excess micromotion, which is one of the major sources of decoherence. See ref.[5] for a detailed discussion on ion dynamics with Mathieu equations analysis.

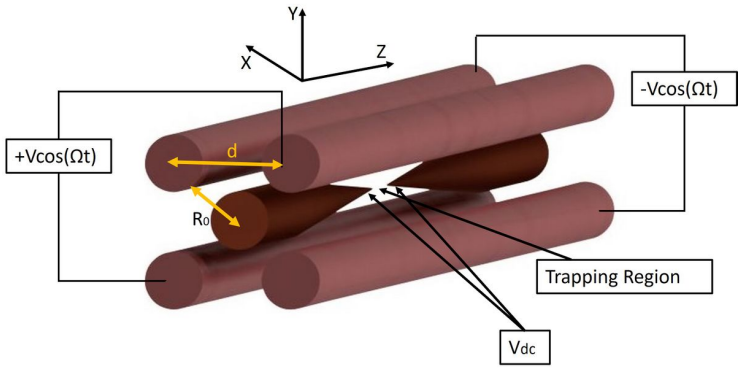

Figure 1.1: Four-rod linear Paul trap of QITI lab [1]:
One pair of DC needles with voltage V_{dc} for axial confinement and two pairs of RF electrodes with oscillating voltages $\pm V\cos\Omega t$ arranged diagonally and anti-diagonally have voltages oscillating out of phase, providing an pondermotive potential. This configuration has RF null in the z-axis, ideally aligned with the DC needles. Electrodes voltages are configured to make $\omega_x, \omega_y \gg \omega_z$ so that a chain of ions equilibrate with each other under the external electric field and mutual Coulomb potential so that they got crystallized along the needle direction.

Ion Loading The process by which ions are produced from an atomic source and subsequently confined within a pondermotive potential is termed *loading*. Popular techniques achieve ion generation by first producing a neutral atomic vapor. This is commonly done

either with resistively heated oven[6] or laser ablation[7, 8, 9]. Once generated, these neutral atoms traverse into the potential well, arriving at the targeted trapping region. Here, ionization can occurs through many means. For hyperfine qubits like $^{171}Yb^{+}$ specifically, the two-photon ionization process offers a distinct advantage of isotope selectivity. A more detailed discussion of this method can be found in Section1.2.2.

Trap System The trap is kept in an ultra-high vacuum (UHV) chamber. For the system shown in Fig.1.2 specifically, the chamber vacuum level is around 2e-11 mbar. The volume of the chamber is around 1L. At room temperature, the system is estimated to have a background collision event between a residual hydrogen atom and an ion qubit occurs at minutes-to-hours level. The background collision rate increases linearly with the number of ions in the chain. With a 25-ion chain, we experimentally observed that a destructive collision event that melts the ion chain due to excessive heating occurs around 5 minutes.

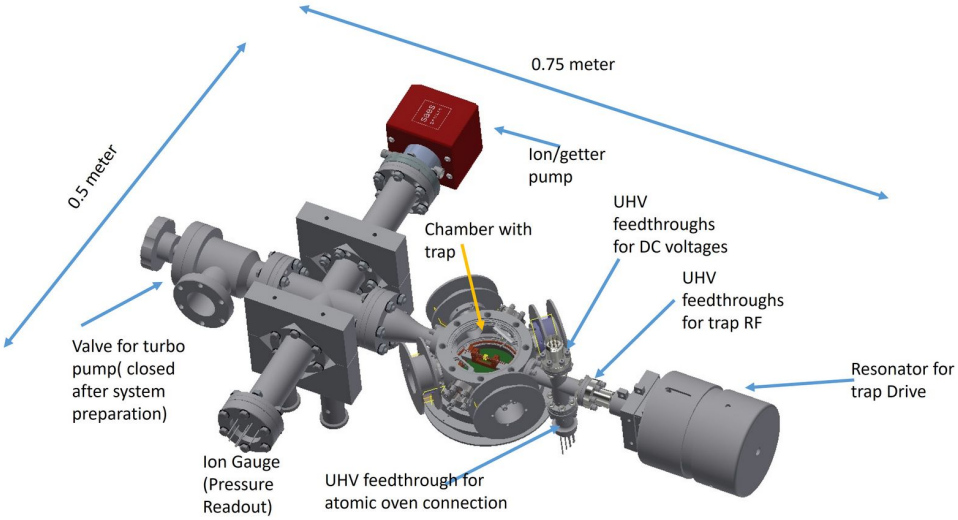

Figure 1.2: QITI four-rod linear Paul trap full system:
In the middle of the figure, it shows the vacuum chamber with a four-rod trap installed. On the left of the chamber are the vacuum connection parts of a turbo pump, a getter pump, and a ion gauge. For this system specifically, the vacuum level is at 2e-11 mbar. To the right of the chamber, the resonator provides the oscillation frequencies of the electrode voltages.

1.1.1 Motivation for PLA Loading

To use a trapped ion quantum computer, one must start with a good loading scheme. Good qualities include: loading time is faster than the chain melting time; does not contaminate the internal electronics that may lead to extra heating.

We have already decided to use two-photon ionization to make ions out of the neutral atoms because of its isotope selectivity. The question is what is a better way to generate the neutral atoms.

Oven Loading We started with a resistively heated oven. See Fig.1.3 for an example of oven design in the QITI lab. The metal source with a cross section of 2 mm diameter is inserted into a high resistance stainless steel tube. When the tube is heated when current is flowing through, the metal target is also heated. When the vapor pressure of the Yb metal exceeds the vacuum level, atomic vapor is generated.

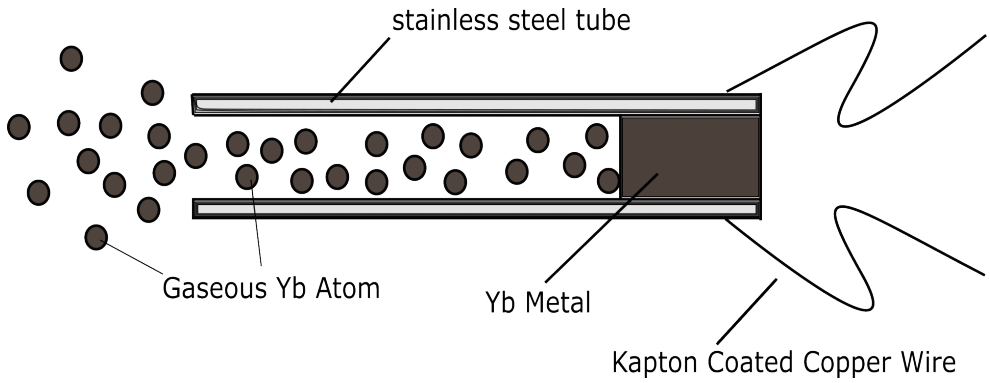

Figure 1.3: Sketch of oven target:
Kapton coated copper wires deliver current that flows through the stainless steel tube, which is resistively heated and conducts heat to the Yb metal target. Vaporized Yb atoms escape the metal surface and travel through the tube toward the trap.

Although being a conventionally popular and easily implementable method, oven loading has many disadvantages.

First, the oven loading is slow. Resistively heated oven takes tens of seconds to several minutes to heat up and cool down, which is on the time scale of the chain melting time mentioned in Section.1.1. Second, the oven is usually designed to heat up the entire atomic source, which tends to create excessive atomic flux, which is not ideal for quantity-limited

sources due to rareness and/or radioactivity, such as $^{133}Ba^{+}$. Excess atomic flux also raises concerns about electrode contamination. Unwanted deposition on electrodes may deprecate the calibrated static electric field, pushing ions away from the RF null thus introducing heating.

Figure 1.4: Sketch of the ablation target:
An ablation laser is focused down to 100 μm spot size at the metal target, which is a few millimeters in width and length. When laser fluence is above the ablation threshold, a plume that contains neutral Yb atoms is generated.

An alternative method that uses pulsed laser ablation is gaining its popularity nowadays.

Pulsed Laser Ablation (PLA) Pulsed laser ablation (PLA) is a widely-used technique in numerous applications, such as thin film deposition and laser machining. This method compresses optical energy into short pulses obtaining high peak power to ablate material from a surface, creating vapor or plasmas. When using nanosecond pulse lasers to ablate metal targets, the light-material interaction time exceeds the electron-lattice coupling timescale, which is typically on the order of picoseconds. This allows sufficient time for heat to transfer from electrons to the lattice, leading to the initial melting followed by the evaporation of the metal [10, 11].

PLA loading process is on the milliseconds scale – many groups have experimentally shown single pulse loading of one or more ions with nanosecond pulsed lasers at tens of hertz repetition rate [8, 7]. Moreover, lasers can be focused down to hundreds or even tens of micrometer-sized spots, heating up a small surface area instead of the whole atomic source, the sizes of which are often on the millimeter level. Ablation loading is also more

controllable in a way that one can tune not only the spot size, but also the laser power. When ablation fluence, the ablation energy per unit area, is close to the ablation threshold, fewer total particles but higher neutral to ion ratio can be achieved [12]. See Fig.1.4 for a simplified sketch of ablating Yb metal target.

In summary, ablation loading is about three orders of magnitude faster than common oven loading techniques and reduces excessive atomic flux with a smaller heating surface area. PLA loading is promising for our trap in the future when long chain (> 50 ions) loading is needed.

1.2 Loading Yb Ions

This section introduces $^{171}Yb^{+}$ qubit definition and its controlling lasers for general interests. Then, we will talk about the two-photon ionization process for the Yb element, explaining how to achieve isotope selectivity with 399 nm transition, which is the first step of the two-photon ionization and also the transition for neutral atom detection. Finally, I will discuss in detail the 399 nm transition broadening effects, building some understanding for the simulation work and experimental results discussion later.

1.2.1 $^{171}Yb^{+}$ Qubit

$^{171}Yb^{+}$ has nuclear spin of $\frac{1}{2}$ so it presents hyperfine splitting under an external magnetic field. The qubit is encoded in the two clock states of the hyperfine ground level $^2S_{1/2}$. Conventionally, they are defined as

$$|0\rangle := {}^2S_{1/2}\,|F=0, m_F=0\rangle \tag{1.4}$$

$$|1\rangle := {}^2S_{1/2}\,|F=1, m_F=0\rangle \tag{1.5}$$

Lasers used for $^{171}Yb^{+}$ qubit manipulations are mostly in UV and optical regimes.

- 369 nm is used for Doppler cooling, qubit state detection, and qubit initialization via optical pumping.
- 355 nm is used for coherent qubit control such as qubit rotation and qubits entanglement
- 760 nm and 935 nm are used for repumping from unwanted F and D states.

See Fig.1.5 for a more complete energy level diagram with the mentioned transitions highlighted.

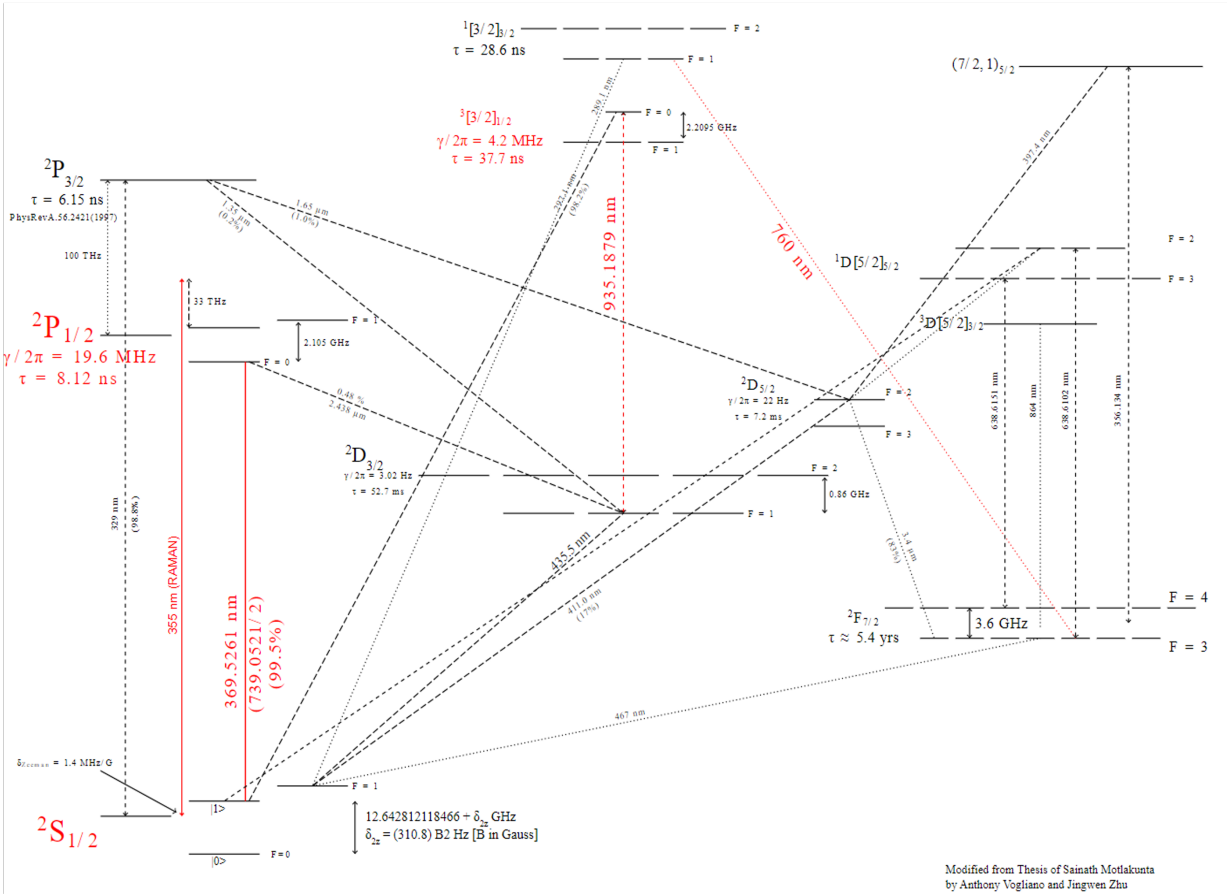

Figure 1.5: Yb level diagrams

1.2.2 Two-photon Ionization of Yb Atom

There are many stable Yb isotopes in nature. Major ones include ^{170}Yb, ^{171}Yb, ^{172}Yb, ^{173}Yb, ^{174}Yb, ^{176}Yb. See Fig.1.6 for a natural abundance histogram of these major ones. ^{171}Yb is the qubit isotope and ^{174}Yb being the most abundant species and having no hyperfine structure is often used for initial setup and subsequent system debugging.

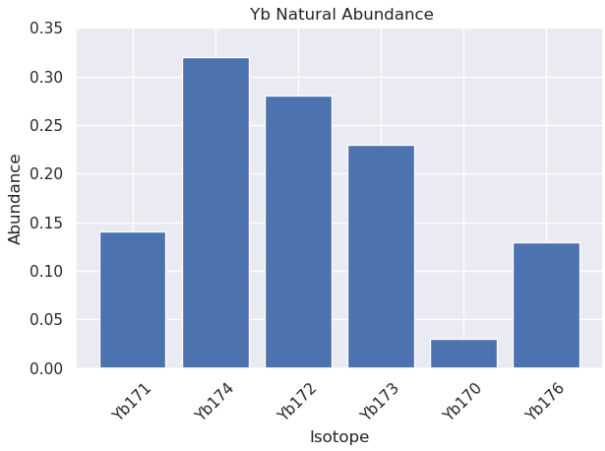

Figure 1.6: Yb natural abundance ratio for several main isotopes

A two-photon ionization scheme [13] helps us to load and identify the correct isotope. Fig.1.2.2 shows a level diagram of the two-photon ionization process. It involves two steps:

1. Excite the atom from $^1S_0$ to $^1P_1$ with 399 nm. This transition exists in neutral atoms $^1S_0$ is a two-electron state. So the 399 nm is also used for neutral Yb atom detection. In experiments, we collected 399 nm fluorescence to confirm the existence of neutrals.

2. Excite atom from $^1P_1$ to continuum with a wavelength lower than 394 nm, i.e. photons with energy higher than 3.15 eV – first ionization energy of Yb is 6.25 eV and 399 nm photon energy is 3.1 eV. Two of our existing lasers, 369 nm and 355 nm, are eligible for this step.

There are many reasons to go for a two-photon ionization scheme: 1. first ionization energy 6.25 eV corresponds to $<$ 200 nm laser, which is a difficult wavelength to get; and 2. The first step with 399 nm transition enables isotope selectivity. 399 nm transition has a natural linewidth of $\sim 2\pi \times 28$ MHz. See in Fig.1.7b that the isotope shifts are mostly

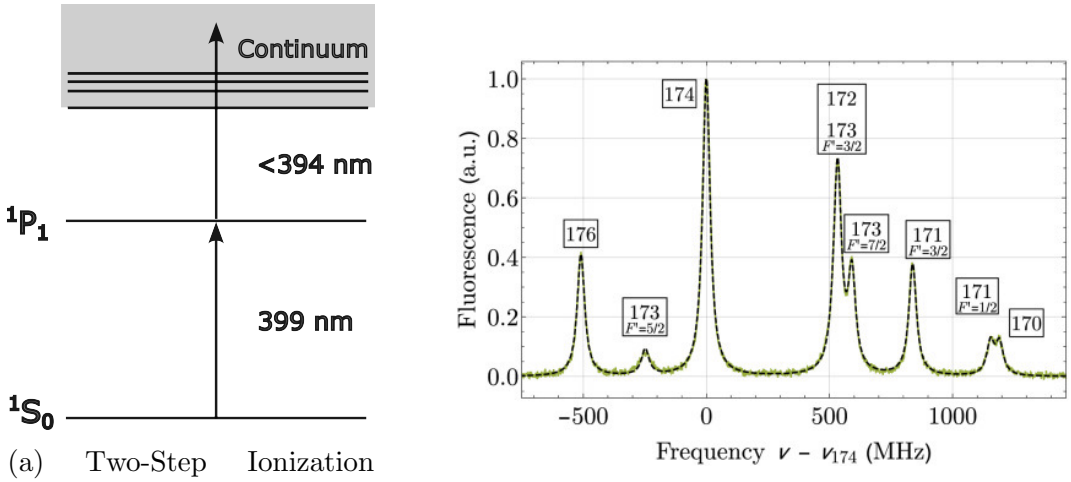

(a) Two-Step Ionization Scheme

(b) 399 nm Transition Isotope Shifts [14]

Figure 1.7: Two-step ionization and 399 nm transition isotope shifts

hundreds of MHz apart. If other transition broadening effects are minimized, such as the power broadening and Doppler broadening, we can load desired isotope by setting the 399 nm laser at the correct isotope peak frequency.

Thus, it is important to understand the broadening effects of the transition line and find a way to minimize them to an extent that isotope peaks do not overlap and isotope selectivity can be achieved.

1.3 399 nm Transition Broadening

The 399 nm $^1S_0 \rightarrow {}^1P_1$ transition has a natural linewidth $\Gamma = 2\pi \times 28$ MHz, lifetime $\tau = 5.5$ ns, and wavelength of $\lambda = 398.911$ nm.
Its saturation intensity [13] can be calculated by $I_{\text{sat}} = \frac{\pi hc}{3\lambda^3\tau} = 60$ mW/cm^2 where h the Planck's constant, c the speed of light in vacuum.

The scattering rate follows the formula

$$R_{\text{sc}} = \frac{\Gamma}{2} \frac{I/I_{\text{sat}}}{1 + I/I_{\text{sat}} + 4\left(\frac{\Delta}{\Gamma}\right)^2} \tag{1.6}$$

where I the incident light intensity, I_{sat} is the saturation intensity of the transition, Δ is the total detuning of the incident light from the atomic transition, including laser detuning

Δ_{399} and Doppler shift Δ_{DS}.

$$\Delta := \Delta_{399} + \Delta_{DS} \tag{1.7}$$

1.3.1 Power Broadening

The scattering rate equation in Eq.1.6 resembles a Lorentzian form:

$$R_{\text{sc}} = \frac{\Gamma}{2} \frac{I/I_{sat}}{1 + I/I_{sat}} \frac{1}{1 + \frac{4\Delta^2}{(1+I/I_{sat})\Gamma^2}} \tag{1.8}$$

where the last term is a Lorentzian distribution with a full width half maximum (FWHM) of $\frac{\Gamma\sqrt{1+I/I_{sat}}}{2}$. This shows that linewidth is dependent on laser power I. Fig.1.8 shows the line shape in different ratios of I/I_{sat}.

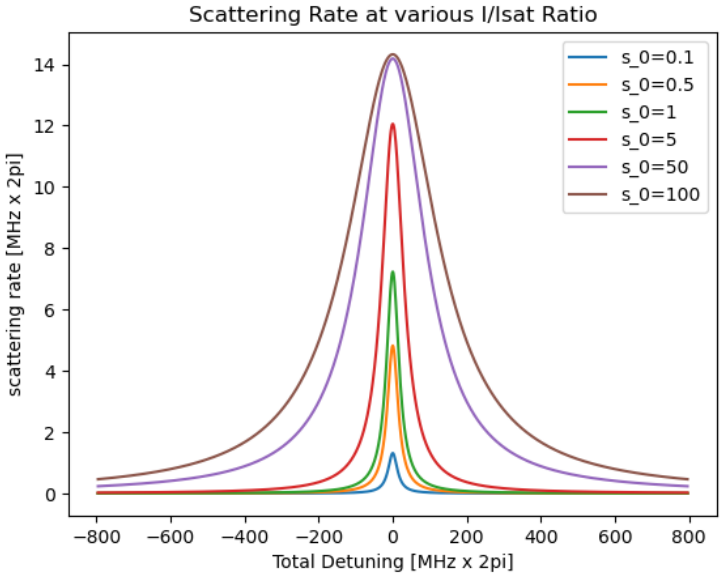

Figure 1.8: Scattering rate of 399 nm transition vs total detuning:
This graph plots the Lorentzian $R_{sc}(\Delta, I)$ curves at several $s_0 = I/I_{sat}$ ratios. The peak R_{sc} values at $\Delta = 0$ approaches to a supremum of $\Gamma/2$ as $s_0 \to \infty$. However, large s_0 also broadens the distribution.

1.3.2 Doppler Broadening

Doppler Shift If the atom has velocity component v in the propagation direction of the 399 nm beam, the light frequency f observed by atom will be shifted by δf from the actual frequency f_0 due to Doppler effect:

$$\delta f = \frac{v}{c} f_0 \tag{1.9}$$

where c the speed of light, and f_0 the unshifted light frequency observed in lab frame. The observed frequency f is a function of v:

$$f = f_0 + \delta f \tag{1.10}$$

$$= f_0(1 + \frac{v}{c}) \tag{1.11}$$

Doppler Broadening When a group of gaseous atoms is at thermal equilibrium, its velocity V is a random variable (rv) distributed as Maxwell-Boltzmann distribution (MB) with a center-of-mass speed v_{cm} and a characteristic temperature T:

$$V \sim MB(v_{cm}, T) \tag{1.12}$$

In one-dimensional case, MB takes the form of a Gaussian distribution:

$$MB_{1d}(v_{cm}, T) = \sqrt{\frac{m}{2\pi kT}} e^{-\frac{m(v-v_{cm})^2}{2kT}} \tag{1.13}$$

$$= G(v_{cm}, \sigma_v) \tag{1.14}$$

So that

$$V \sim G(v_{cm}, \sigma_v) \tag{1.15}$$

with a standard deviation of

$$\sigma_v = \sqrt{\frac{k_b T}{m}} \tag{1.16}$$

Let F represents the rv of observed frequency in Eq.1.11. Let $h_V(v)$ and $h_F(f)$ denotes the probability density function (pdf) of rv V and F separately. We can transform $h_F(f)$

from $h_V(v)$:

$$h_F(f) = h_V(v)\frac{dv}{df} \tag{1.17}$$

$$= h_V(v(f))\frac{c}{f_0} \tag{1.18}$$

$$= \frac{c}{f_0}G(c(\frac{f_{cm}}{f_0} - 1), \sqrt{\frac{k_bT}{m}}) \tag{1.19}$$

$$= \frac{c}{f_0}G(f_{cm}, \frac{f_0}{c}\sqrt{\frac{k_bT}{m}}) \tag{1.20}$$

where $f_{cm} = f_0(1 + v_{cm}/c)$ Given that the velocity V follows a Maxwell-Boltzmann (MB) distribution, the observed light frequency F exhibits a broadened probability density function. This broadened distribution for F is also Gaussian in nature:

$$F \sim G(f_{cm}, \sigma_{DB}) \tag{1.21}$$

where

$$\sigma_{DB} = \frac{f_0}{c}\sqrt{\frac{k_bT}{m}} \tag{1.22}$$

which represents the Doppler broadening width of the frequency distribution.

Chapter 2

Numerical Simulation of 399 nm Fluorescence

There are many variables that can affect the fluorescence signal level, such as the plume temperature that characterizes the velocity distribution, the 399 nm frequency and the Doppler shift that affect the scattering rate, the photon detector's time window, etc, making the experimental data complicated to be fitted with a closed form formula. Building a simulation tool helps to understand the effect of each parameter and gain insights on the expected signal level, the direction to reduce broadening effects, and estimate some parameters when compared to experimental data. In this chapter, I begin by defining the velocity distribution of atoms and introducing notations for subsequent discussions in Sec.2.1. I then progress from calculating the single atom fluorescence using the Monte Carlo method in Sec.2.2 to generating a full spectrum with various experimental parameters in Sec.2.3.

2.1 Velocity Distribution of Atoms

The commonly used dynamics model for ablation generated plume is a shifted one-dimensional Maxwell-Boltzmann distribution [12, 15] for the velocity v that is perpendicular to the ablation target surface, which takes the form of a Gaussian distribution,

$$V \sim G(v_{cm}, \sqrt{\frac{k_b T}{m}}) \tag{2.1}$$

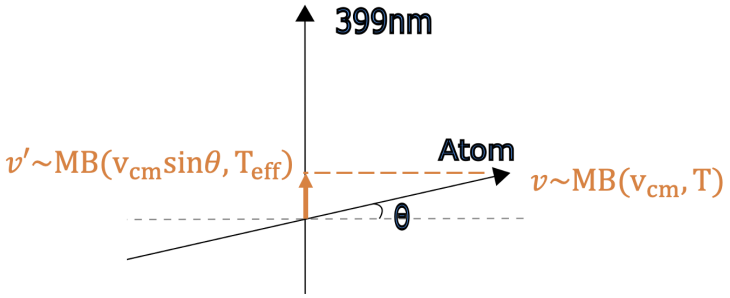

Figure 2.1: Alignment geometry

as introduced in Sec.1.3.2. So the atoms' velocities projection in the 399 nm direction

$$V' = V \sin\theta \tag{2.2}$$

where θ is the misalignment angle defined in Fig.2.1, also follows an one-dimensional Maxwell-Boltzmann distribution in the shape of a normal distribution

$$V' \sim G(v_{cm} \sin\theta, \sqrt{\frac{k_b T_{eff}}{m}}) \tag{2.3}$$

with an effective temperature $T_{eff} = T \sin^2\theta$ that characterizes the distribution spread in the 399 nm laser propagation direction. Discussions in previous Sec.1.3.2 explains that normal distributed velocity components in 399 nm direction leads to a Doppler broadening of observed 399 nm light frequency,

$$\sigma_{DB} = \sqrt{\frac{k_B T_{eff}}{mc^2}} f_0 \tag{2.4}$$

which convolutes with other broadening effect to further broaden the 399 nm transitions line.

2.2 Single Atom Fluorescence

Knowing the expected total fluorescence emitted by a single atom as it traverses the ionization beam, we can estimate the atom population from later experiments.
Single atom fluorescence can be calculated as:

$$\#\text{photon} = \text{Scattering Rate} \times \text{Scattering Time} \tag{2.5}$$

As discussed in Sec.1.3, the scattering R_{sc} is a function of 399 nm laser detuning Δ_{399} and Doppler shift Δ_{DS}. For atoms with velocity v traversing 399 nm beam at an misalignment angle θ, Δ_{DS} can be calculated as

$$\Delta_{DS} = \frac{v \sin\theta}{c} f_0 \tag{2.6}$$

Let d the beam diameter of 399 nm at the intersection with atomic flux. The interaction time between neutral atoms and 399 nm laser is approximately d/v at small misalignment angles. Thus, the total fluorescence is:

$$\#\text{photon} = R_{sc}(\Delta_{399}, \Delta_{DS}) \times \frac{d}{v} \tag{2.7}$$

For a fixed θ and Δ_{399}, the Eq.2.7 is simply a function of atom velocity v:

$$\#\text{photon} = h(v) = R_{sc}(v) \times \frac{d}{v} \tag{2.8}$$

Since the velocity follows a Maxwell-Boltzmann distribution as describe before, we are essentially looking for a expectation value of the fluorescence photon number $\mathbf{E}[h(V)]$:

$$\mathbf{E}[h(V)] = \int_0^\infty h(v_i) f_V(v_i) dv \tag{2.9}$$

where $f_V(v)$ is the pdf of velocity.

To avoid the complicated integration, we wanted to do Monte Carlo simulation. Using a method called Inverse Transform Sampling, we were able to draw random samples from any (non-)uniform distribution, so that Eq.2.9 was turned into a simple average problem, which can be solved by Monte Carlo simulation:

$$\mathbf{E}[h(V)] = \frac{1}{N} \sum_N h(v_i) \tag{2.10}$$

where v_i are i.i.d. (independent and identically distributed) samples from $f(v)$. Fig.2.2 shows examples of random sampling results.

2.2.1 Distribution Settings

Similar research [7] reported fitted parameters of $v_{cm} \sim 500$ m/s and a plume temperature $T \sim 500$ K at the ablation threshold ~ 0.3 J/cm^2. An educated guess of our parameters corresponding to our ablation fluence F is based on energy conservation, $v_{cm} \propto \sqrt{F}$ and $T \propto F$. In later paragraphs, we will show the simulation results in or close to the following three settings.

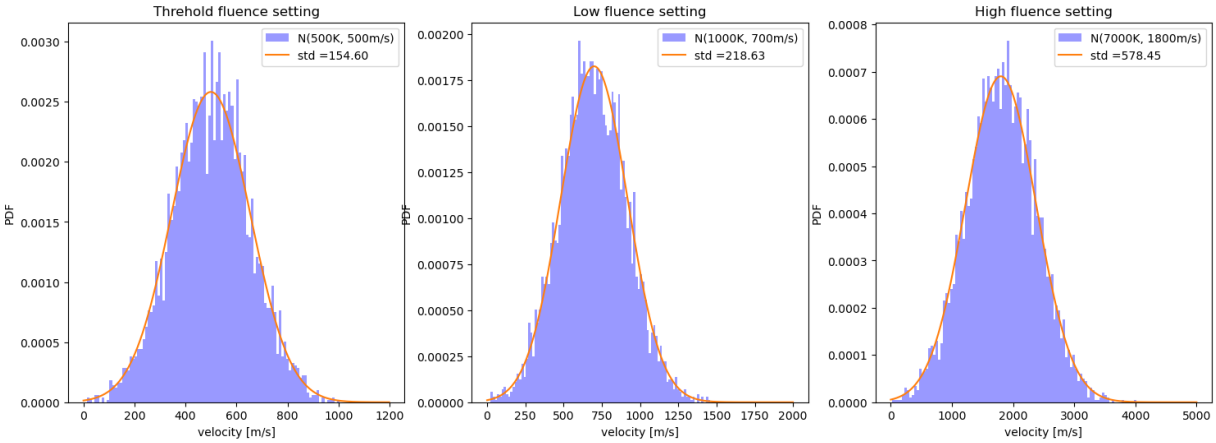

Figure 2.2: Random sampling from 1D Maxwell-Boltzmann distribution (Eq.2.1)

- Threshold fluence setting at 0.3 J/cm^2: $MB(500 \text{ m/s}, 500 \text{ K})$.
- Low fluence setting at 0.6 J/cm^2: $MB(700 \text{ m/s}, 1000 \text{ K})$.
- High fluence setting at 4 J/cm^2: $MB(1800 \text{ m/s}, 7000 \text{ K})$.

See random sampling from Maxwell-Boltzmann distributions at three setting in Fig.2.2.

2.3 Spectrum Simulation Results

Besides the expected Doppler broadening, later experiment revealed notable plume divergence, as detailed in 4.1. Subsequently, we will present the spectrum simulations under two scenarios:

1. Without plume divergence, where all atoms are presumed to travel consistently in the direction defined by the misalignment angle.
2. With plume divergence, incorporating a uniformly random angle within a 15° half-angle to the initial misalignment angle.

Let's observe the transition line behaviour first.

Transition Line Simulation Fig.2.3 shows the a transition lineshape at various small misalignment angles, three fluence settings, and parallel comparison between plume with and without divergence. At smaller misalignment angles, the divergence-induced broadening becomes predominant, overshadowing the Doppler broadening and leading to a reduced signal at equivalent fluence settings.

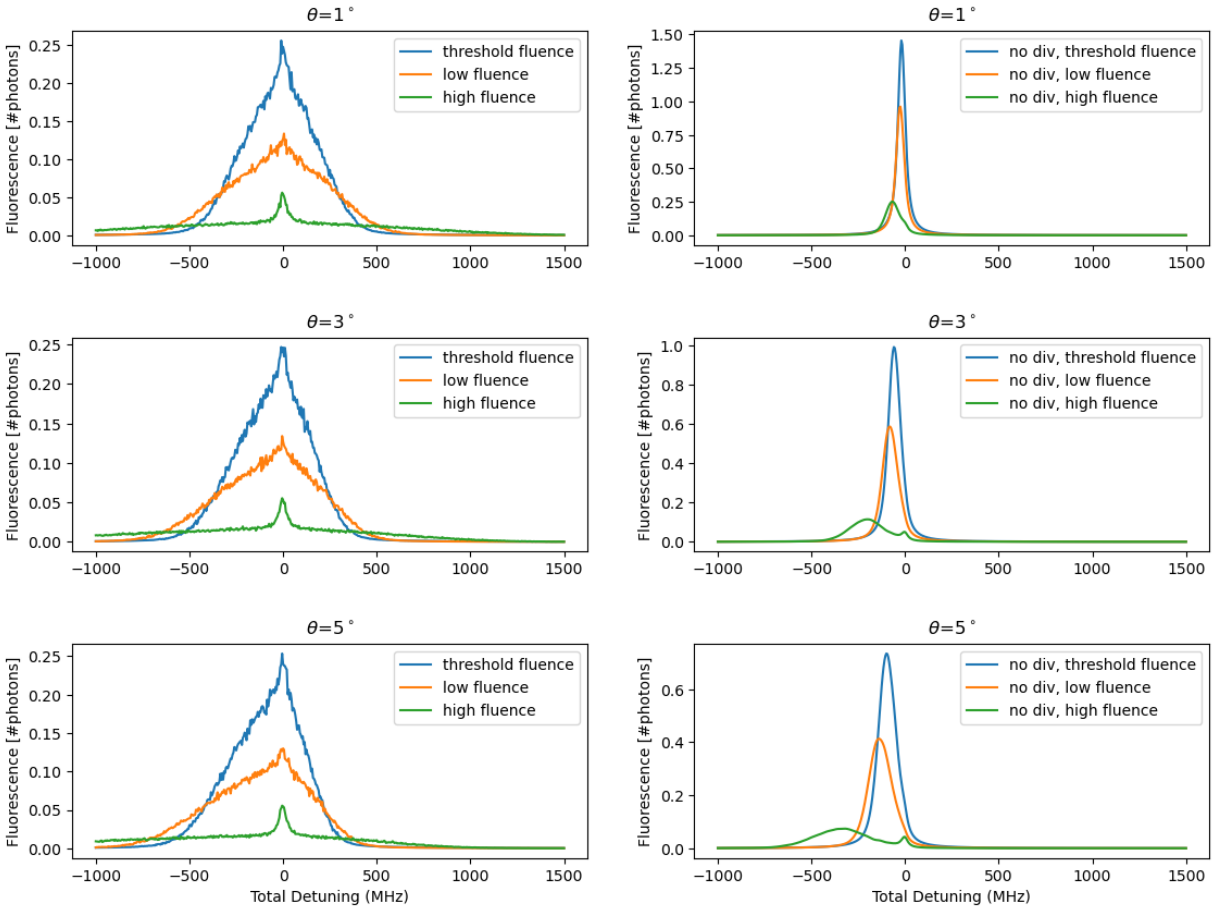

Figure 2.3: Transition line broadening at three misalignment angles with and without plume divergence:

Each simulated spectral line is calculated from $N = 500$ samples and $I_{399} = I_{sat}$.

Full Spectrum Simulation Given the natural abundance of each isotope, we integrated the transition lines for all isotopes generated using the Monte Carlo method. Fig.2.4 shows spectra of plume with and without divergence in perfect alignment under low fluence

setting. Due to discrepancies in the randomly generated diverging angles between each run, we present three results from each setting to provide a broader view of potential outcomes. We observe that even at a misalignment angle of 0°, the spectrum with a diverging plume loses selectivity between the two nearest ^{172}Yb and ^{173}Yb isotope peaks. Furthermore, situations where the more distantly spaced ^{170}Yb and ^{171}Yb peaks merge are also evident, (Fig.2.4, top). Conversely, simulations with a non-diverging plume consistently produce isotope-resolvable spectra, (Fig.2.4, bottom).

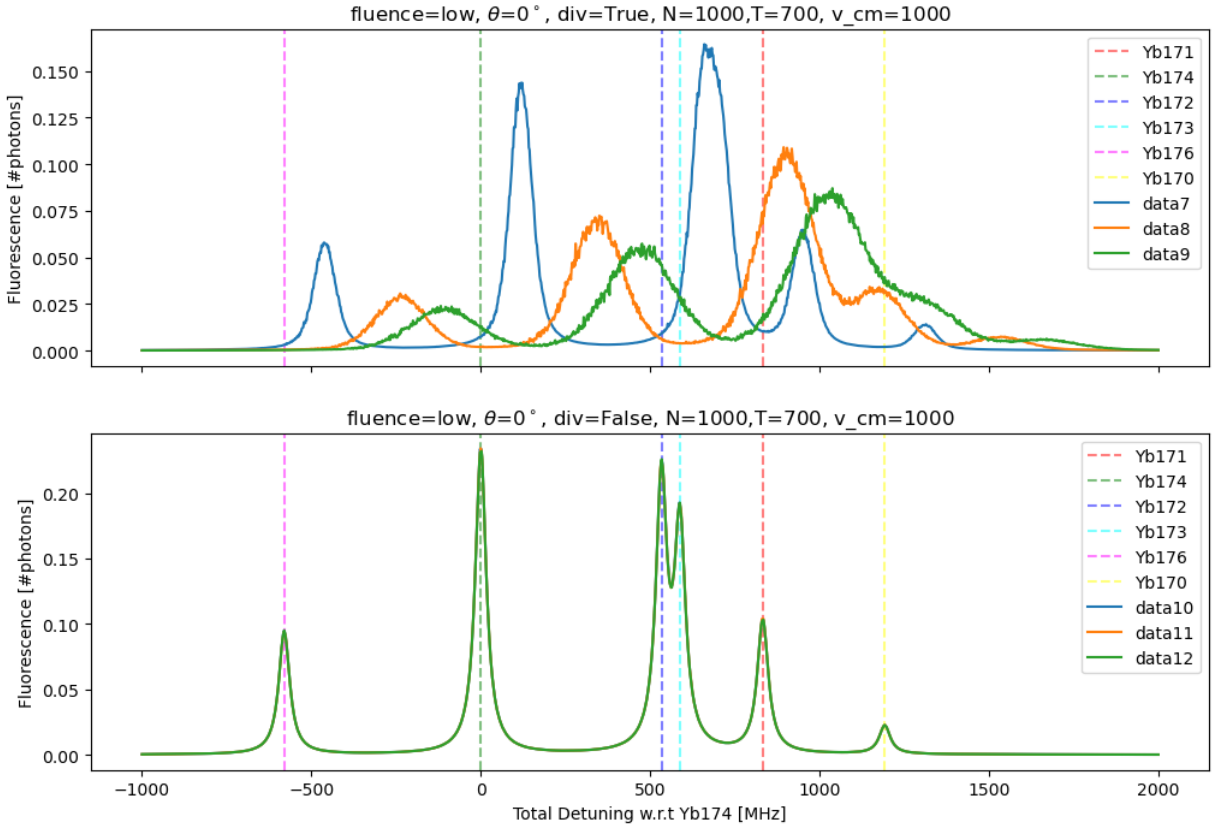

Figure 2.4: Low fluence full spectrum simulation in perfect alignment:
Each plots shows three simulation results under the same plume and fluence settings calculated from $N = 1000$ samples and $I_{399} = I_{sat}$. The figure above was simulated with plume divergence and figure below was without.

Fig.2.5 presents a comparison of full spectra at several small misalignment angles under low ablation fluence settings. It is evident that a diverging plume exhibits greater Doppler

shifting and broadening compared to a non-diverging plume at equivalent small angles and fluence levels. With a divergence of 15° half-angle, misalignments at 1° to 3° do not result in significant differences; however, substantial broadening and shifting can be observed at 5°. In contrast, the effects of Doppler broadening are more consistent for non-diverging plumes. The proximate peaks of ^{172}Yb and ^{173}Yb remain relatively distinguishable at a 1° misalignment.

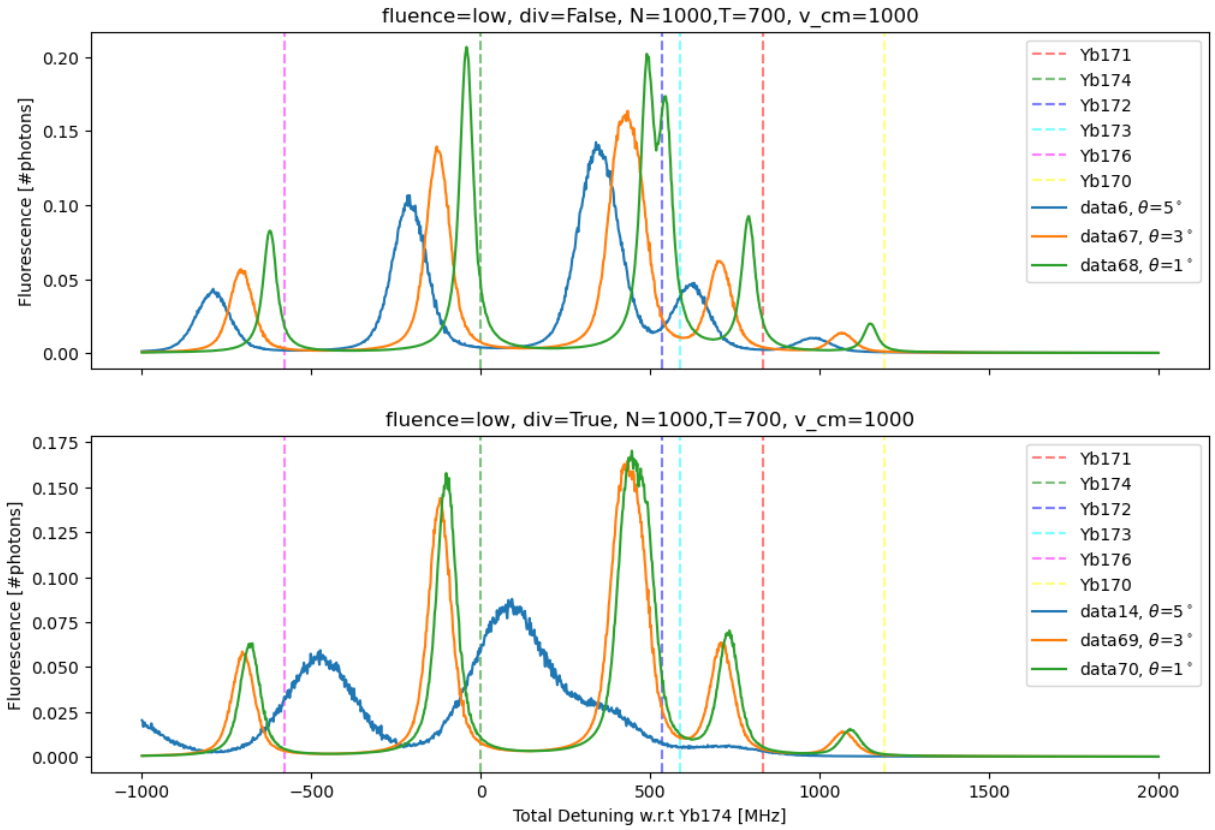

Figure 2.5: Low fluence full spectrum simulation at small misalignment angles, $\theta = 1°, 3°, 5°$

.

2.4 Summary

One consistent observation from all simulations is that we can expect about 0.02 to 0.2 photon from single atom with our experimental setup. Also, plume divergence dominates

the transition broadening at small angles. Small alignment adjustment by 1° in experiment can result in significant differences in isotope peak distinguishability.

Chapter 3

The Experimental Setup

Our ablation laser is a nanosecond pulsed infrared (IR) laser as introduced in Sec.3.1. The laser output has a fluence of 1.2 J/cm^2. Shrinking the beam size by a mere factor of two, the fluence can exceed the laser-induced damage threshold (LIDT) of optics coating, which is typically in the range of $5 - 10$ J/cm^2 according to Thorlabs. If not considering LIDT of the optics and detectors carefully, we risked burning important pieces, especially when attempting the fiber-coupled delivery approach. The LIDT of general optics components is discussed in Sec.3.3. A specific discussion of optical safety for the fiber-coupled path is in Sec.3.5, including a recommended fail-safe power monitor using a fiber coupler/splitter.

3.1 The Falcon 1.57 μm Ablation Laser

We chose the 1.57 μm Falcon laser by Lumibird for ablation. Fig.3.2 shows the physical unit outlook. Falcon has a pulse width of 4 ns and a pulse energy of about 5 mJ. The repetition rate can be set from 1 to 40 Hz. See all important parameters in Table.3.1. The pulse energy can be linearly adjusted with the diode current setting. See the pulse energy calibration in Fig.3.3.

Parameter	Value
Type	Diode-pumped solid state Nd:YAG laser
Wavelength	1574 nm
Rep rate	1 - 40 Hz
Pulse width	4 - 5 ns
Beam diameter	0.96 mm (collimated)
Beam profile	Gaussian
Pulse energy	4.74 mJ (typical)
Energy density	1.2 J/cm^2 (collimated)
Peak power	1.25 MW
Average power	200 mW

Figure 3.1: Laser parameters

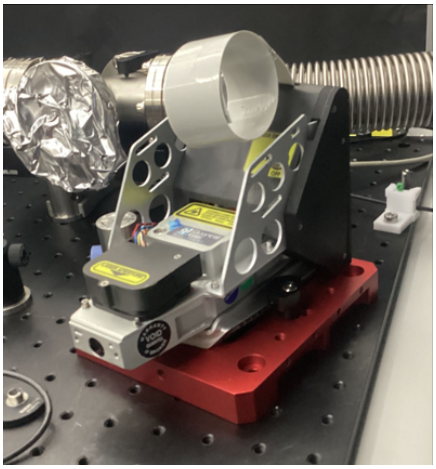

Figure 3.2: Falcon laser unit

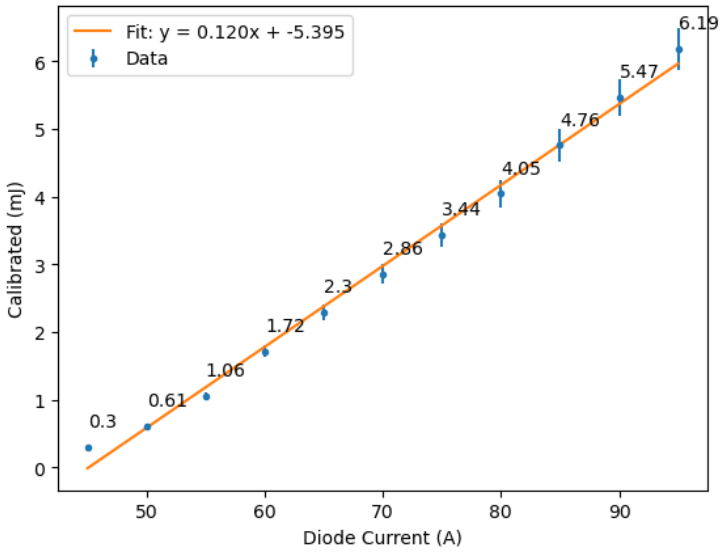

Figure 3.3: Pulse energy calibration:
Pulse energy is measured with Thorlabs ES111C pyroelectric sensor which has 5% uncertainty. The beam was attenuated by OD=1.39 to protect the sensor. The lasing threshold is 45 A below which the the laser has no stable output. The laser outputs from 300 μJ to 6.19 mJ.

3.2 Optics

The proposed setup encompasses the delivery of a 1.57 μm ablation beam, the delivery of the 399 nm beam, and an imaging system for fluorescence collection. The entire optical system is modularized across two breadboards, the *preparation board* and the *ablation board*, distinguished based on their functionalities. section.3.2.1 explains breadboards layout with a top view diagram. Imaging system, which was aligned on top of the chamber, is explained in section.3.2.2 with a side view diagram. An alternative *fiber-coupled* path is installed between the two boards. This setup was tested separately from main experiments in Chap.4, which were done with free space delivery, as feasibility test of the fiber delivery approach. See discussions on fiber-coupled delivery in Chap.3.5.

3.2.1 Breadboards Layout

The *preparation board* serves for upstream ablation laser fluence control to ensure optical safety and facilitates guide beam merging, which aids in alignment with the IR laser. The *ablation board* manages the control of downstream ablation fluence through beam focusing and additional attenuators to regulate the actual ablation fluence on the target. Furthermore, this board oversees the delivery of the 399 nm beam, hosts the imaging system, and accommodates the vacuum chamber containing the ablation target. The free space delivery can be switched to a fiber-coupled delivery module for different test purposes. When the fiber-coupled path is chosen, a fail-safe live energy monitor based on an avalanche photodiode (APD) can be put in action. For a detailed explanation of the optical layout, see Fig.3.4.

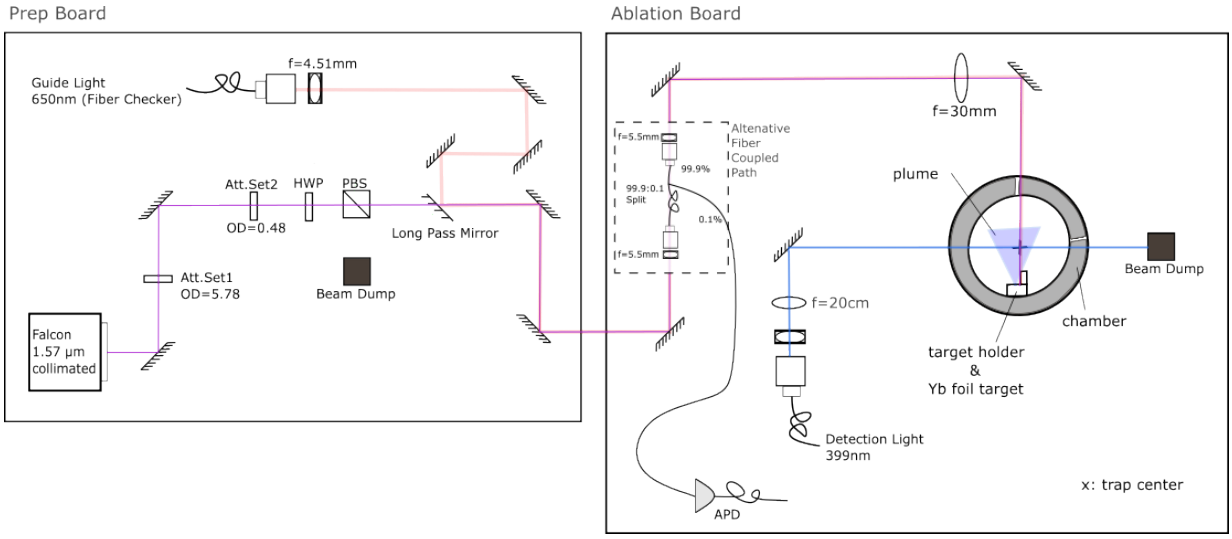

Figure 3.4: Preparation board, ablation board, and fiber-coupled module layouts: The *Preparation board* controls the energy of the 1.57 μm ablation with a half-wave plate (HWP) and a polarization beam splitter (PBS). It co-aligns the 1.57 μm ablation beam with a 650 nm guide beam from a laser checker through a long-pass dichroic mirror. Attenuator sets are installed to safeguard optical components for free space delivery (Attn.Set2) and fiber-coupled delivery (Attn.Set1&2). On the ablation board, the co-aligned ablation beam is focused with a 30 cm lens and aligned onto the target with a spot size of 550 μm in diameter and a Rayleigh range of 150 mm. This board also handles the focusing and alignment of the 399 nm beam. It is first collimated to 1 mm diameter beam after fiber and then focused by a 20 cm lens to the trap center with a spot size of 102 μm in diameter and Rayleigh range of 20 mm. 399 nm laser power before attenuation is 80 μW. The vacuum chamber also sits on the ablation board. The imaging system is installed on top of the chamber, aligned to the trap center marked by a cross sign in the purple triangle.

3.2.2 Imaging System

The purpose of the imaging system is to collect as much atom fluoresced 399 nm photons as possible and align the gathered light with the detector sensor. For this purpose, the imaging quality is not critical. With available optics components at hand, I combined two identical 1"-diameter plano-convex lenses of focal length $f = 50$ mm to get an effective focal length of 25 mm. The size of the chamber prevents any working distance smaller than 4 cm. With this setup, I was able to get a numerical aperture (NA) of 0.254. See the

geometry sketch and relevant parameters in Fig.3.5.

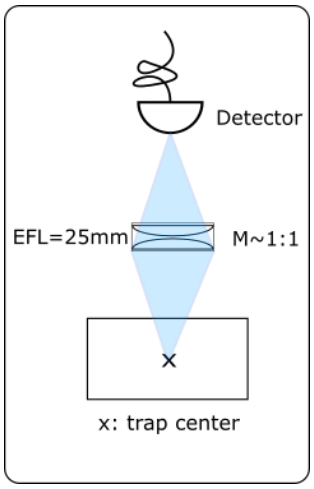

(a) Imaging Optics Sketch

Parameter	Value
Working Distance	50 mm
Aperture Size	1”
EFL	25 mm
NA	0.254
Magnification	1

(b) Imaging Optics Parameters

Figure 3.5: Imaging optics and parameters

Detectors

Initially, an avalanche photodiode (APD, Thorlabs APD440A2) was used to retrieve fluorescence signals but was later switched out with a photomultiplier tube (PMT, Hamamatsu H10682-210) for better signal-to-noise ratio (SNR). A spec comparison is listed Table.3.1. The noise level of the APD at maximum gain was measured roughly 30 mV. Given a

Model	**Hamamatsu H10682-210**	**Thorlabs APD440A2**
Sensitivity/Responsivity	4.4×10^5 /s/pW	max 25 A/W
Dark Count / Noise	Max 100/s	0.8 pW @ max Gain
Gain	N/A	1.25×10^9 V/W
Active Area	8 mm	1mm

Table 3.1: Comparison of the Hamamatsu H12775 and Thorlabs APD440A2

signal of 500 mV, which corresponds to a signal-to-noise ratio (SNR) of approximately 20, the inferred input optical power is around 400 pW. Under the same input optical power conditions and with an integration time of 1 μs, the PMT can, in theory, yield close to 180 counts with fewer than 1 dark count. This offers a notably better SNR compared to the APD. Furthermore, the active area of the PMT is 64 times greater than the APD's, leading to a significant increase in photon collection efficiency.

3.3 Laser Induced Damage Threshold (LIDT)

High power laser can cause damage to materials via various processes[16, 17]. Table 3.2 summarizes the dominating damage mechanisms in different pulse length regimes. In nanosecond regime, the damage can be dielectric and thermal. Most lenses and mirrors we use are coated fused silica. The coating can have significant lower LIDT compared to bulk fused silica for many reasons, such as dirt or scrathes on the surface, local heat absorption spots due to coating defects, etc. Generally, LIDT is expressed in units of [W/cm^2] for continuous-wave (CW) light, and in [J/cm^2] for pulsed light. Considering pulsed laser, LIDT of coated lenses are typically about 10 J/cm^2.

Pulse width	**Mechanism**
CW	Thermal effect, heat absorption, electron-lattice dynamics
ns pulse	Thermal effect, dielectric breakdown
<10ps pulse	Nonlinear effect, such as multiphoton absorption, multiphoton ionization, tunnel ionization, and avalanche ionization. Coulomb explosion.

Table 3.2: LIDT mechanism in different pulse width regime

However, the exact mechanisms of laser induced damage is still largely undeterministic. Even for the same material, the LIDT can vary with the laser wavelength, fluence, pulse width, etc. Manufacturers, such as Thorlabs and Edmund Optics, often provide LIDT specifications measured under specific test laser conditions on their spec sheets. With this information, one can apply some empirical formulas to estimate an adjusted LIDT based on specific parameters.

Adjusted LIDT

For example, when dealing with nanosecond pulsed lasers, Thorlabs gives a LIDT measurement with their laser of wavelength λ_0 and pulse width τ_0. The adjusted LIDT for using a another laser of λ, τ is calculated as:

$$\text{Adjusted LIDT} = \text{LIDT}\sqrt{\frac{\lambda}{\lambda_0}}\sqrt{\frac{\tau}{\tau_0}} \tag{3.1}$$

A similar adjusted LIDT formula can be found on Edmund Optics website with more stringent conditions. Since almost all our components were from Thorlabs, I used Thorlabs' formula to calculate adjusted LIDT for our components. See Table 3.3.

Description	**Part number**	**Adjusted LIDT (J/cm^2)**
HWP	WPH05ME-1550	7.16
PBS	PBS254	3.16
Beam Sampler	BSF10-C	4.74
ND Filters	NENIR10B-C	4.74
Long-Pass mirror	DMLP950	3.08
Mirror (protected gold)	PF10-03-M01	1.54
Fiber	N/A	Take bulk silica LIDT
Collimators	C105TMD uncoated	Take bulk silica LIDT
Pyroelectric Energy Sensor	ES111C	0.3

Table 3.3: LIDT of critical optics components for Falcon laser

3.4 Chamber, Vacuum, Target

The intended tests for this project do not require trapping potentials. Thus, I used an empty vacuum chamber. The chamber was turbo pumped to 1e-6 to 1e-7 mbar level. The ablation target is a natural abundance Yb metal foil with thickness of 0.125 mm cut into a 3 mm by 4 mm size. The target is held in place by a screw on the target holder.

3.5 Fiber Collimation Module

Fiber LIDT We use SMF28 fiber for ablation laser delivery. See Table.3.4 for fiber specifications. SMF28 is a silica based fiber. From several sources[18, 19, 16, 17], I inferred that the LIDT of this fiber, if surface is cleaned, should be close to that of bulk silica at around 350 J/cm^2 at 1550 nm. It was also experimentally verified that the bare-end SMF28 was burnt at around 320 J/cm^2 within 100 pulses. Fig.3.7 shows pictures of undamaged and damaged fiber tip. To protect fiber from laser damage, one should be very careful to keep the fiber tip scratches and dust free. We also set 250 J/cm^2 as the upper limit of fiber input fluence, which corresponds to 105 μJ with 10.4 μm mode field diameter (MFD).

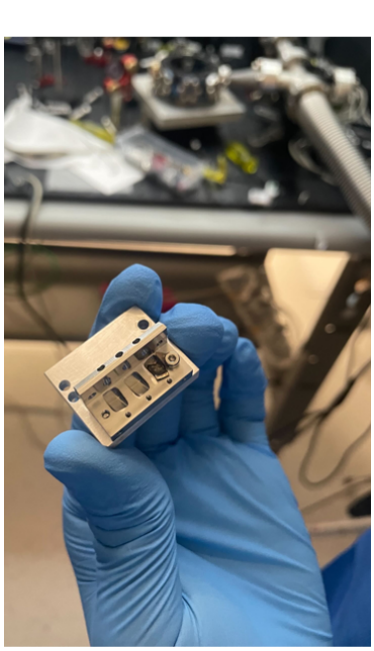

(a) Target foil installed in target holder

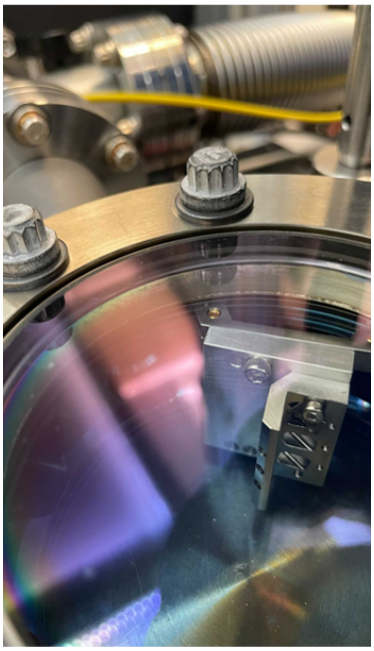

(b) Target holder mounted on chamber rim

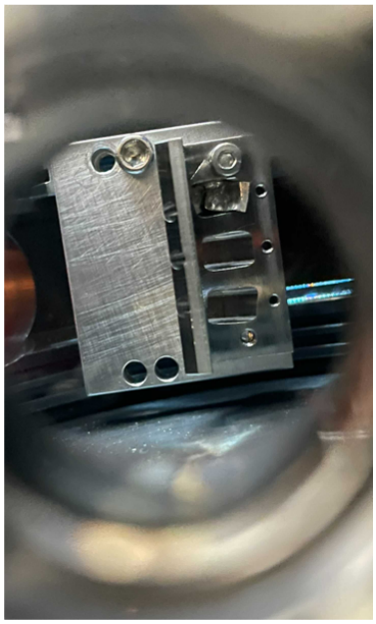

(c) Target and its holder seen through a viewport

Figure 3.6: Target, target holder, and chamber assembly

Fiber Coupling Optics A f=5.5 mm uncoated aspheric lens (Thorlabs C105TMD) focuses the 1.09 mm diameter beam down to 10.4 μm MFD. The Attn.Set2 with OD=0.48 is required to bring the 300 μJ laser output (diode current 45A) to 100 μJ, ensuring fiber safety.

Detector for Fiber Coupling Detecting the initial coupled light turned out to be quite challenging. Given our input energy was merely 100 μJ, the required sensitivity must be at the 1-2 μJ level, if not at the nJ level. Three types of detectors were considered:

1. **Thermal sensors:** They lack the necessary timing resolution for ns pulsed laser coupling.
2. **Pyroelectric sensors (ES111C):** Gives reliable readings only for pulse energy greater than 5 μJ. The readings are inconsistent for pulses below 2 μJ, which makes them unsuitable unless we fortunately achieve at least 5% initial coupling efficiency.

Fiber type	Corning SMF-28 Ultra
MFD	10.4 ± 0.5 μm @ 1550 nm
LIDT	300∼350 J/cm^2 (i.e. about 120∼150 μJ)
Input/Output Collimator	Thorlabs C105TMD, f = 5.5 mm

Table 3.4: Important Specs of fiber collimation

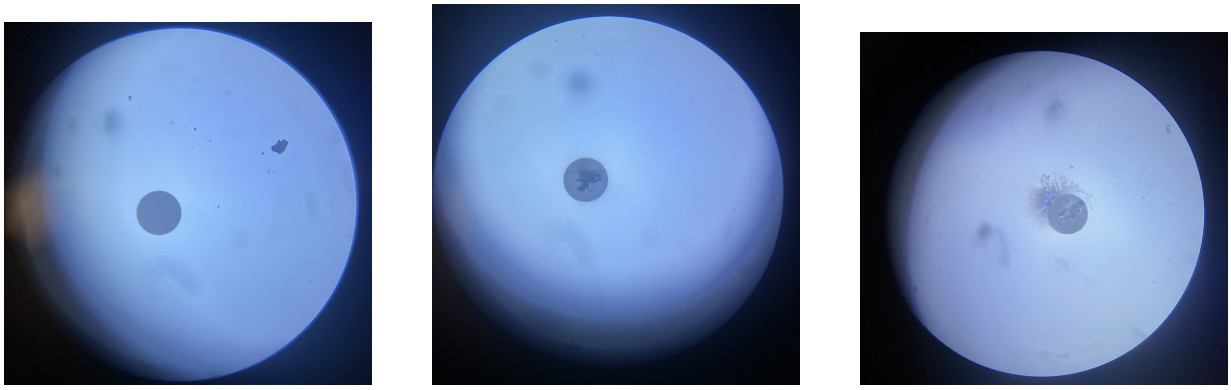

(a) Undamaged bare-end fiber

(b) Deliberately damaged bare-end fiber

(c) Unknowingly blasted end-capped fiber

Figure 3.7: Laser-damaged and undamaged fiber

3. **Photon detector (Thorlabs DET08CFC):** This emerged as the most suitable option. It has GHz level bandwidth and can detect pJ level energy.

The Thorlabs DET08CFC photon detector was finally chosen as the optimal solution for fiber coupling. Its maximum output is 2 V, which corresponds to an optical energy of 180 pJ. Thus an additional Attn.Set1 of OD = 5.78 is needed for detector safety. See component layout in Fig.3.4.

Fiber Coupling Procedure The C105TMD collimator has a 150 μm focal shift between 650 nm light and 1.57 μm light. We can utilize this effect to get a kickstart on 1.57 coupling by optimizing 650nm coupling efficiency. Making sure that the guide beam and ablation beam are overlapped over a few meters distance, I first optimized the coupling for 650 nm beam, so that the optimal fiber position is approximately 150 μm further away. Using translational stage to slowly increase distance between collimator and fiber tip, while iteratively adjusting the two mirrors before the fiber to optimize coupling for the ablation

laser. Eventually, I got 30% coupling efficiency. The efficiency can be improved if the mode is matched better.

Fiber-Coupler Energy Monitor Instead of using a common one-output fiber, I used a 99.9% : 0.1% fiber splitter to make an in-situ, live, and fail-safe energy monitor for the ablation laser. The 99.9% output is used in the main experiment for ablation, see setup in Fig.3.4. The 0.1% output is connected to APD with -25dB fiber attenuators for APD safety. See Fig.3.8 for a monitor's signal.

Figure 3.8: Coupler power monitor signal

Oscilloscope	DS1102E
Trigger	Slope
Acquisition	PeakDetection
Measurement	Vpp/Vmax, Vmin
Time Resolution	50 ms

Table 3.5: DS1102E setting for retrieving APD signal

3.6 Summary

To conclude, for the ablation experiment, we have set up optics for free space ablation beam delivery that is able to reach a maximum fluence of 4 J/cm^2 with a beam size of 550 μm in 1/e^2 diameter at the ablation target, an imaging system with NA = 0.25, and a vacuum chamber at 1e-6 to 1e-7 mbar pressure level. For future system planning, we have thoroughly studied and confirmed feasibility of bare-end single-model fiber coupling and achieved 30% coupling efficiency, which can be improved with better mode matching.

Chapter 4

Results and Discussion

In this chapter, I begin by presenting the camera-captured fluorescence signals from neutral atoms in Sec.4.1. Subsequently, in Sec.4.2, I discuss the results from the ablation spot lifetime experiment, which provides a stable baseline of fluorescence signal from same ablated spot. Following that, I will present and discuss the results of both the PMT integration time experiment in Sec.4.3 and the 399 nm spectrum scan experiment in Sec.4.4. With understandings from previous simulation work (Chap.2), I will give an estimated atom population, atom velocity distribution, and a percentage of trappable atoms given a specific trap depth using the inferred distribution. Two sets of data with a high ablation fluence of 4 J/cm^2 and a low ablation fluence of 0.7 J/cm^2 will be shown for comparison.

4.1 Neutral Atom Signal

The purpose of this experiment is to qualitatively confirm the existence of neutral Yb atoms in the ablation-generated plume.

Fig.4.1 shows camera images during the ablation process. We could see an obvious blinking stripe when the ablation laser was pulsing and the 399 nm laser was parked near the resonance frequency. This proved that there are neutral atoms generated by laser ablation.

The camera field of view is approximately 5.5 mm by 7.5 mm. The fluorescence stripe's spanning the entire image indicated that plume divergence was not negligible. Based on the setup configuration, I estimated that the divergence half-angle was at least 15°.

(a) background (b) starts fluorescing (c) strong fluorescence

Figure 4.1: Fluorescence detection with camera:
Ablation laser fluence was set at 4 J/cm^2. 399 nm frequency was parked around the resonance frequency of ^{174}Yb. Camera model is a FLIR BFS-PGE-120S4M-CS. It has a field of view was about 5.5 mm by 7.5 mm. All images are taken with same exposure time, gain, and all other camera settings.

4.2 Lifetime of Ablation Spots

The ablation process naturally diminishes the target material, leading to a decline in the signal with accumulated pulse counts on the same ablated spot. For meaning analysis of later experiments whose scanning parameters, such as 399 nm laser detuning, also affects fluorescence level, a stable signal baseline is desired. This experiment sought for a consistent fluorescence signal by either identifying a pulse count range where fluorescence variations remain within one standard deviation, or modeling the fluorescence signal decay regarding the number of ablation pulses.

In subsequent experiments, data points were gathered either within the stable pulse count range or were corrected using the decay model. This ensures that any observed signal decrease arises solely from the 399 nm laser being off-resonance, attributed either to the laser detuning or the Doppler shift.

For both sets of data at two fluence settings, the ablation laser repetition was set at 10 Hz. The PMT integration time was experimentally adjusted to approximate the maximum signal value, while also roughly minimizing the time duration. Achieving the best signal-to-noise ratio (SNR) was not a critical concern for this experiment, as the constant background counts would simply be incorporated as a bias term in the mathematical model for decay.

High Fluence The results for high fluence at 4 J/cm^2 are shown in Fig.4.2. Although the curves are more than 1 standard deviation away from each other, they share common features. The curves increase within the first 6000 pulses and then decay which can be fitted with an exponential decay model:

$$y = Ae^{-t/\tau} + B \tag{4.1}$$

where τ is what we refer to as the lifetime of an ablation spot.

Within the initial 8,000 pulses, the PMT counts remain largely unaffected by decay. Although exhibiting an increasing tendency, the standard deviation ranges overlap approximately 80% between data points. In subsequent experiments (Sec.4.3, 4.4) conducted at this fluence level, data were collected within the first 8,000 pulses where fluorescence signal is at a stable level when all scanning parameters are fixed.

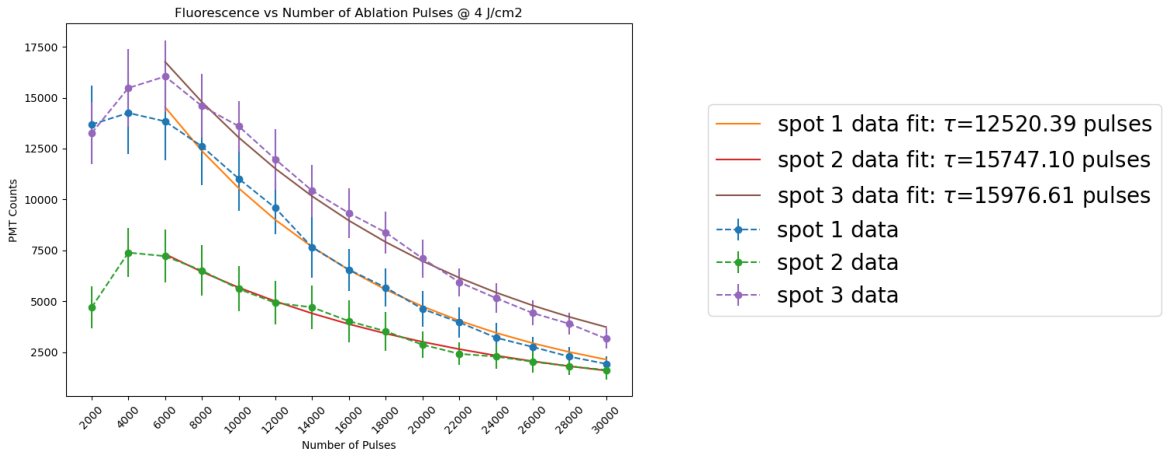

Figure 4.2: Ablation spot lifetime at high ablation fluence
Each data point represents the mean and standard deviation of 100 measurements.

Low Fluence The results for low fluence at 0.7 J/cm^2 are shown in Fig.4.3. At this fluence, we observed that the curves for different spots are close within one standard deviation. Unlike the high-fluence data, the exponential decay model did not fit any part of the curve. So, a fourth-order polynomial was used to fit the curves:

$$y = Ax^4 + Bx^3 + Cx^2 + Dx^1 + Ex^0 \tag{4.2}$$

The model with parameter averaged from the two fitted results was used for correction of later experiment (Sec.4.3, 4.4). The lifetime of the ablation spots is approximately 1,000 pulses where the fluorescence decrease to half of the initial level.

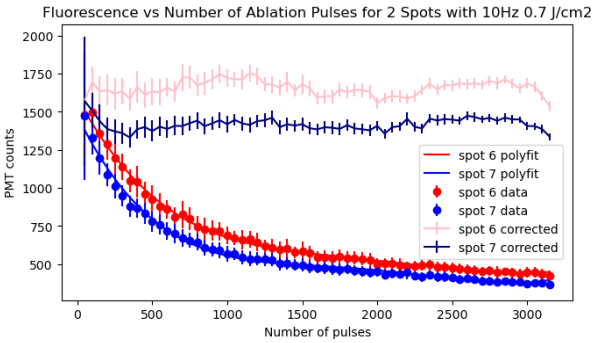

	Spot 6	Spot 7	Average
x^4	5.26e-11	7.02e-11	6.14e-11
x^3	-4.33e-07	-5.57e-07	-4.95e-07
x^2	1.31e-03	1.59e-03	1.45e-03
x^1	-1.86e+00	-2.03e+00	-1.94e+00
x^0	1.60e+03	1.48e+03	1.54e+03

Figure 4.3: Ablation spot lifetime at low ablation fluence:
Each data point represents the mean and standard deviation of 50 measurements. The solid red and blue lines represent decaying fluorescence collected on two separate spots, fitted with a fourth-order polynomial (Eq.4.2). The semi-transparent red and blue lines depict the corrected counts using the fitted polynomial parameters presented in the table to the right.

4.3 PMT Integration Time

The PMT was triggered to start collecting counts for an integration time τ synchronously when an ablation pulse was sent out. The background counts increased linearly with τ whereas the fluorescence signal would saturate after a certain time when nearly all atoms have flew over the interaction region with the 399 nm laser.

This experiment aimed to find the optimal PMT integration time such that most of the total fluorescence could be captured while having a sufficiently small background count.

High Fluence Observations from the high fluence data, as depicted in Fig.4.4a, indicate that PMT count rises sharply within the initial 1 ms. It continues to increase, although at a slower rate, until 2 ms. While the signal shows an upward trend, the Signal-to-Noise Ratio (SNR) experiences a rapid decline within this 2 ms interval. For later experiments, we chose the PMT integration time of 1 ms. This choice allowed us to capture approximately 80% of the total fluorescence while maintaining a satisfactory SNR at about 100.

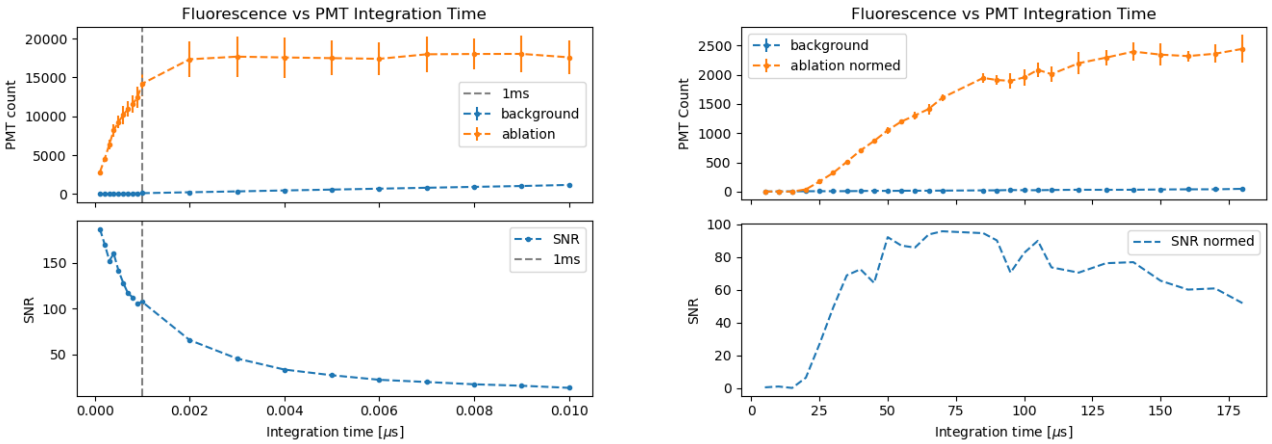

(a) High Fluence

(b) Low Fluence

Figure 4.4: PMT Count vs PMT Integration Time:
Left (High Fluence): Each data point represents the mean and standard deviation of 50 measurements. We collected data within the first 8,000 pulses to avoid decay. Right (Low Fluence): Each data point represents the mean and standard deviation of 10 measurements. The polynomial model (Eq.4.2) was used for correction.

Low Fluence For the low fluence data, see Fig.4.4b, the PMT count begins to rise from 25 μs and stabilizes by approximately 150 μs. The Signal-to-Noise Ratio (SNR) improves with the signal, peaking within the first 50 μs and plateaus in the range of 70-90 μs. We chose the PMT integration time of 80 μs for later experiments because it captures approximately 80-90% of the total fluorescence while maintaining an optimal SNR about 100.

Given that the sensitivity of the PMT count is $6.1 \times 10^5\,\mathrm{pJ}^{-1}$ at 400 nm, with each atom contributing an average of 0.02 to 0.2 photons, and considering the imaging system's collection efficiency of approximately 2%, we estimate a total atomic population between 10 million and 100 million when the PMT signal registers around 12,000 counts under high fluence settings. Likewise, for a PMT signal of approximately 2,500 counts, the estimated atomic population ranges from 2 million to 20 million under low fluence settings.

The integration plot can also be seen as a cumulative distribution function (cdf) of the traversing time atom spent before leaving the 399 nm beam that is distance L away from the ablation target. Assuming a fixed scattering rate for all atoms, the fluorescence signal

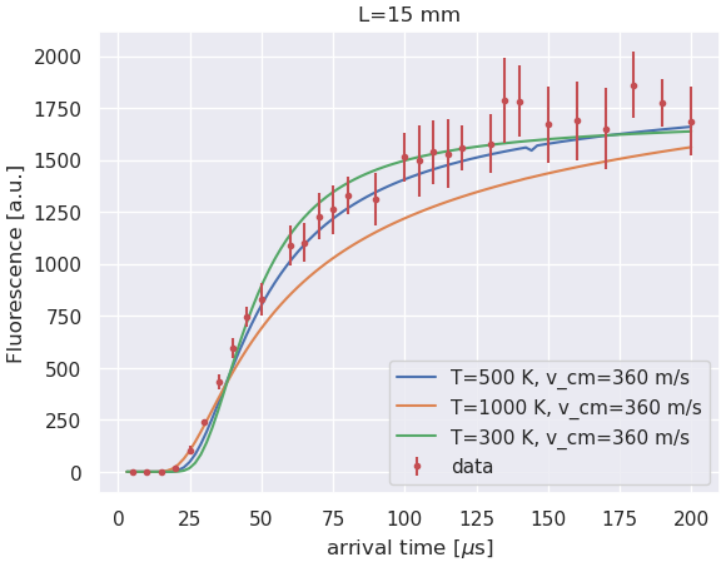

Figure 4.5: Integration time fit with traversing time cdf model

is

$$h(t) = A \times R_{sc} t + B \tag{4.3}$$

$$= A \times R_{sc} \int_0^t t f_T(t) dt + B \tag{4.4}$$

where $f_T(t)$ is the pdf of traversing t:

$$t = \frac{L}{v} \tag{4.5}$$

Having atom velocities pdf $f_V(v) \sim \mathcal{N}(v_{cm}, \sigma_v(T))$ (Eq,1.15), we are able to transform Eq.4.4 into a function of v:

$$h(t) = A \times R_{sc} \int_0^t f_T(t) dt + B \tag{4.6}$$

$$= A \times R_{sc} \int_{L/v}^{\infty} \frac{d}{v} f_V(v) dv + B \tag{4.7}$$

$$= h(v) \tag{4.8}$$

By changing the fitting parameter v_{cm} and plume temperature T which determines σ_v, and manually adjusting amplitude A and bias B, we are able to locate a few settings

that yield signal trend close to the experimental data, Fig.4.5. The optimal setting for integration plot is $v_{cm} = 360$ m/s and plume temperature $T = 500$ K.

4.4 399 nm Spectrum Scan

This experiment was designed to obtain a fluorescence spectrum of the 399 nm transition over an approximate range of ±1 GHz. By fitting the spectrum with a summation of Gaussian profiles

$$y = bias + \sum_i a_i \exp \frac{-(x-\mu_i)^2}{2\sigma_i^2} \tag{4.9}$$

we can estimate the effective temperature in the 399 nm propagation direction from the broadened profile width, Eq.2.4, using

$$T_{eff} = \left(\frac{\sigma_{DB}}{f_l}\right)^2 \frac{mc^2}{k_B} \tag{4.10}$$

We initially performed a spectrum scan using high fluence at 4 J/cm^2. Preliminary analysis of these results indicated significant Doppler broadening effects, which made isotope peaks indistinguishable. This motivated us to change to low fluence at 0.7 J/cm^2, which yielded a more discernible spectrum with reduced Doppler broadening. To further mitigate broadening effects from misalignment, the spectrum scan was also performed at angles of $\pm 1^\circ$ and -1.5° relative to the reference angle.

High Fluence The spectrum scan is shown in Fig. 4.6. The profile nearly plateaued for over 500 MHz due to Doppler broadening. Fitting all possible isotope peaks in the scanning frequency range was not successful. However, we were able to fit with two Gaussians. The width of the central Gaussian gives an effective temperature of 833 K in the direction of 399 nm propagation. We then switched to a low fluence setting expecting less Doppler broadening, thus more distinguishable isotope peaks.

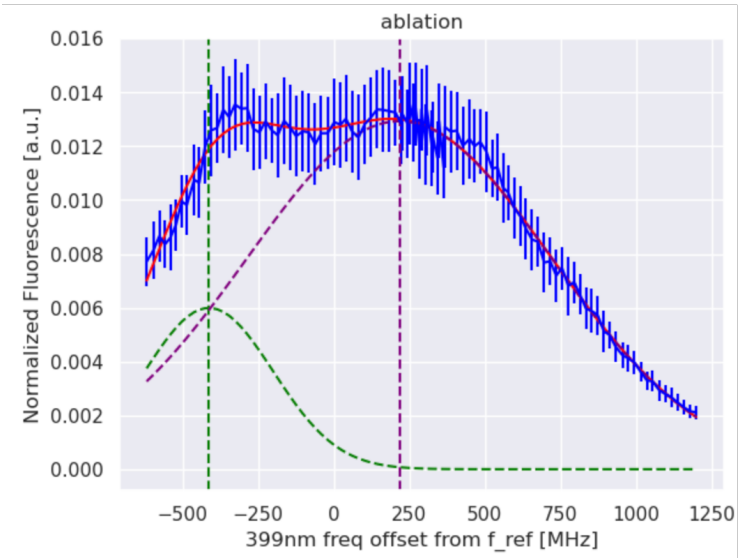

Figure 4.6: High fluence 399 spectrum analysis
Each data point represents the mean and standard deviation of 100 measurements. From two fresh spots with similar initial PMT counts, we collected data within the first 8,000 pulses to avoid decay.

Low Fluence At low fluence, the isotope peaks are more clearly distinguishable when observed at the initial reference angle. Subsequently, we adjusted the misalignment angle to observe variations in Doppler broadening. The curves corresponding to $+1°$ and $-1°$ angles show close overlap, indicating symmetry with respect to the reference angle. In general, all four misalignment angles show similar broadening effect and peak visibility. See Fig.4.7.

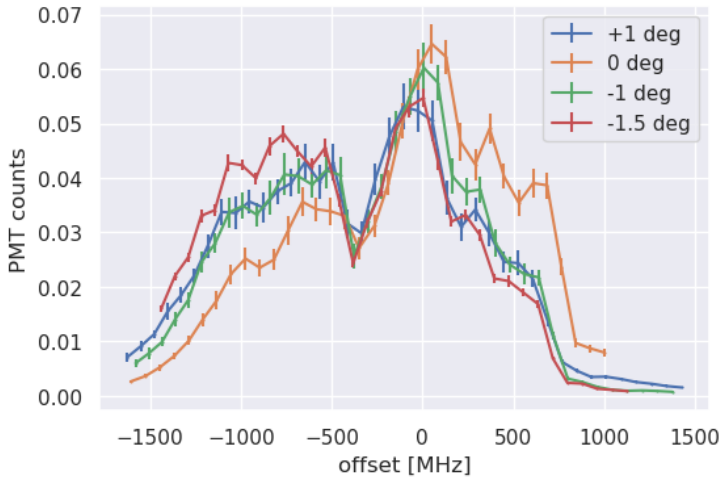

Figure 4.7: Low fluence 399 spectrum analysis:
Each data point represents the mean and standard deviation of 20 measurements. The PMT counts have been corrected using the polynomial decay model. Spectrum scan results conducted at four different misalignment angles are shown.

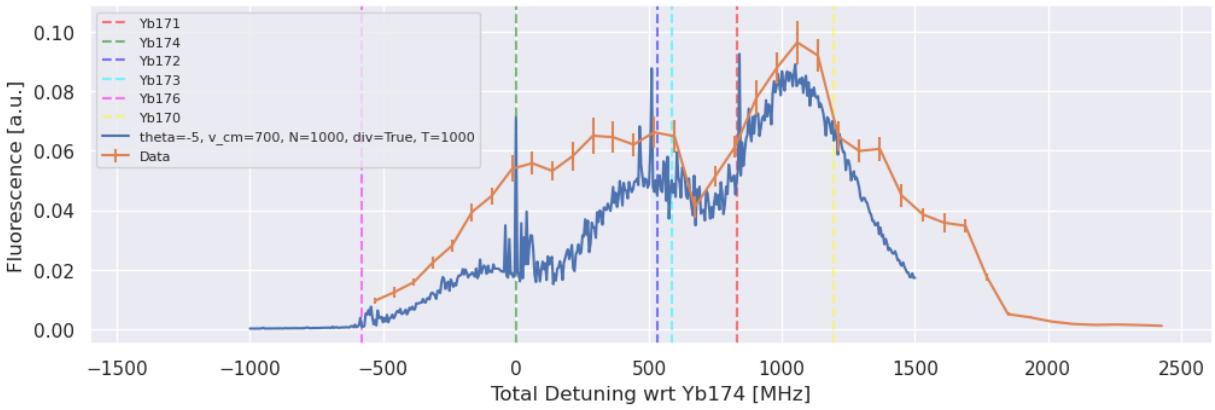

Figure 4.8: Manual fitting with plume divergence spectrum simulation model:
A spectrum were simulated with misalignment angles of $-5°$ using the inferred parameters from the low fluence setting pdf. Each data point in the simulated spectra is an aggregate of 1,000 runs. The experimental data were adjusted in both amplitude and frequency offset positioning to show overlap with the simulated results.

By manually adjusting the simulation model with plume divergence studies in Sec.4.4,

we found an estimate set of parameters when using 15° half angle: plume temperature $T = 1000\,\mathrm{K}$, center-of-mass velocity $v_{cm} = 500\,\mathrm{m/s}$ at low fluence settings. See Fig.4.8.

Having the inferred velocity distribution, we can get a kinetic energy (KE) distribution using:

$$KE = \frac{1}{2}mv^2 \tag{4.11}$$

We estimate that approximately 2.5% of the neutral atoms have kinetic energies below the trap depth of 10 meV, making them trappable within the system. See Fig.4.9.

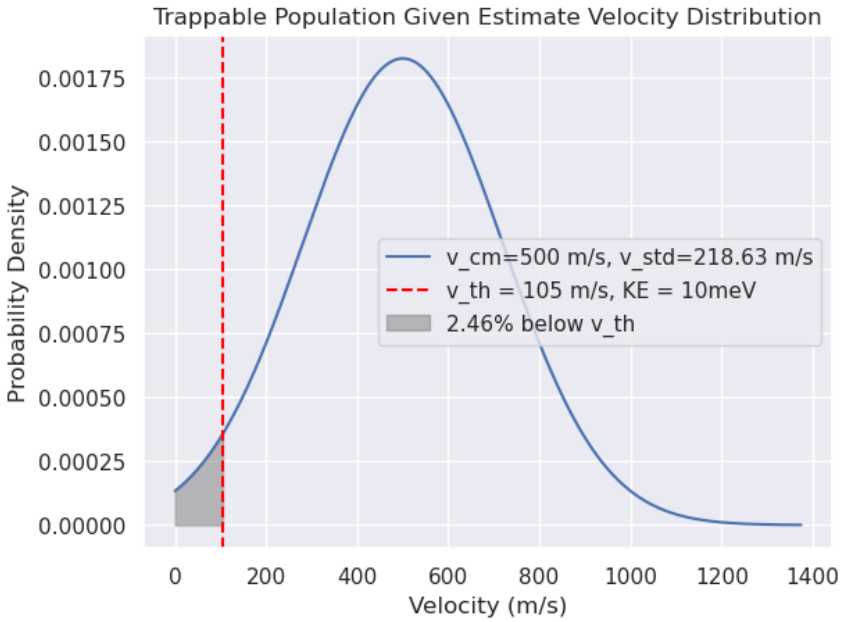

Figure 4.9: Velocity distribution with $v_{cm} = 500$ m/s and $T = 1000$ K
A trap depth of 10 meV corresponds to a velocity threshold of 105 m/s. At this velocity or below, the kinetic energy of the atom is sufficiently low for it to be trapped after ionization. The shown PDF is normalized considering only velocities equal to or greater than 0 m/s.

4.5 Summary and Discussion

Summary To conclude, we have confirmed neutral atom generation with camera and estimated a non-negligible plume divergence of at least 15° half angle. For ablation exper-

iments operated at high ablation fluence (4 J/cm^2), we found a stable pulse count range of initial 8,000 pulses within which fluorescence level vary within one standard deviation and after which the fluorescence exhibits an exponential decay with a lifetime of approximately 15,000 pulses. Optimal PMT integration time was set to be 1 ms with SNR = 100. Fluorescence spectrum with our 399 nm laser at high fluence shows a broadened plateau over nearly 1 GHz range without obvious isotope peaks, indicating huge Doppler shift and broadening effects which motivated same sets of experiments but at a lower ablation fluence.

At low ablation fluence (0.7 J/cm^2), we found that fluorescence signal steadily decays as pulse count increases and the trend can not be described by exponential model. We fitted and corrected the decaying signal with a fourth-order polynomial, and found the lifetime to be approximately 1,000 pulses. The PMT integration time was set to be 80 μs with SNR = 100. The PMT integration time data was also used to fit a cdf of atom traversing time, from which we estimated a plume center-of-mass velocity of v_{cm} = 360 m/s and plume temperature T = 500 K. 399 nm spectrum scan at low fluence is less broadened than at high fluence and we are able to identify 5 individual peaks. Using spectrum simulation tool we built in Chap.2, we found the simulated spectrum with v_{cm} = 500 m/s and T = 1000 K shows good overlap with the experimental data. With these parameters, we also modelled atoms' kinetic energy distribution and estimated a 2.5% trappable population with a trap depth of 10 meV.

Discussion The variation in fitted parameters between the traversing time cdf and the simulation might originate from the absence of divergence considerations in the cdf model. Presently, we favor the parameters determined via the Monte Carlo simulation as it encapsulates a broader range of dynamics in the ablation-fluorescence process such as scattering rate change due to velocity and angle. For a deeper understanding of this inconsistency, we can employ the simulation tool to compute the integration time, utilizing the same atomic profiles that generated the spectral data.

Chapter 5

Summary and Outlook

As a preliminary step towards integrating telecom pulsed laser ablation loading into an Yb ion trap, the author has gained valuable knowledge and empirical insights through the simulation and experimental studies. Specifc experimental achievements include:

- Designed an optics setup that emphasizes laser safety.
- Successfully verified the generation of neutral atoms through preliminary tests.
- Determined the ablation spot half-life to be approximately:
  - 15,000 pulses at high fluence.
  - 1,000 pulses at low fluence.
- Estimated atom populations:
  - 10-100 million with high fluence ablation.
  - 1-10 million with low fluence ablation.
- At the low fluence setting, the plume velocity distribution was roughly characterized with:
  - $v_{\mathrm{cm}} = 500$ m/s, $T = 1000$ K.
  - Above parameters renders 2.5% of trappable atoms, which have kinetic energies below a 10 meV trap depth.

Alongside, the author has also designed and proved feasibility of a fiber-coupled ablation delivery module, achieving 30% coupling efficiency with bare-end fibers. The fiber-coupled module is now serving as an in situ, live-time, and fail-safe ablation power control with the use of a fiber splitter.

In the simulation and experimental analysis, we realized that the plume divergence is a non-neglible source of extra transition line broadening. In our future work, we are going to collimate the ablation generated plume to reduce divergence among atoms, and try to obtain an isotope-resolvable 399 nm spectrum to confirm isotope selectivity.

References

[1] Nikhil Kotibhaskar. Design and construction of an ion trapping apparatus for quantum simulation experiments. Master's thesis, University of Waterloo, 2019. Master's thesis.

[2] B.B. Blinov, D. Leibfried, C. Monroe, et al. Quantum computing with trapped ion hyperfine qubits. *Quantum Information Processing*, 3:45–59, 2004.

[3] C. Monroe, W.C. Campbell, L.-M. Duan, Z.-X. Gong, A.V. Gorshkov, P.W. Hess, R. Islam, K. Kim, N.M. Linke, G. Pagano, P. Richerme, C. Senko, and N.Y. Yao. Programmable quantum simulations of spin systems with trapped ions. *Reviews of Modern Physics*, 93(2):025001, April 2021. Publisher: American Physical Society.

[4] Wolfgang Paul. Electromagnetic traps for charged and neutral particles. *Reviews of Modern Physics*, 62(3):531–540, July 1990.

[5] D. J. Berkeland, J. D. Miller, J. C. Bergquist, W. M. Itano, and D. J. Wineland. Minimization of ion micromotion in a Paul trap. *Journal of Applied Physics*, 83(10), May 1998.

[6] Timothy G. Ballance, Joseph F. Goodwin, Bethan Nichol, Laurent J. Stephenson, Christopher J. Ballance, and David M. Lucas. A short response-time atomic source for trapped ion experiments. *Review of Scientific Instruments*, 89(5):053102, May 2018. arXiv:1710.02489 [physics, physics:quant-ph].

[7] Geert Vrijsen, Yuhi Aikyo, Robert F. Spivey, I. Volkan Inlek, and Jungsang Kim. Efficient isotope-selective pulsed laser ablation loading of ^{174} Yb $^{+}$ ions in a surface electrode trap. *Optics Express*, 27(23):33907, November 2019.

[8] Brendan M. White, Pei Jiang Low, Yvette de Sereville, Matthew L. Day, Noah Greenberg, Richard Rademacher, and Crystal Senko. Isotope-selective laser ablation ion-trap loading of Ba + 137 using a BaCl 2 target. *Physical Review A*, 105(3):033102, March 2022.

[9] R. D. Knight. Storage of ions from laser-produced plasmas. *Applied Physics Letters*, 38(4):221–223, February 1981.

[10] B. N. Chichkov, C. Momma, S. Nolte, F. von Alvensleben, and A. Tünnermann. Femtosecond, picosecond and nanosecond laser ablation of solids. *Applied Physics A*, 63(2):109–115, August 1996.

[11] B. Jaeggi, B. Neuenschwander, M. Schmid, M. Muralt, J. Zuercher, and U. Hunziker. Influence of the Pulse Duration in the ps-Regime on the Ablation Efficiency of Metals. *Physics Procedia*, 12:164–171, January 2011.

[12] J. B. de Matos, M. G. Destro, C. A. B. da Silveira, and N. A. S. Rodrigues. Neutral atomic jet generation by laser ablation of copper targets. *Review of Scientific Instruments*, 85(8):083505, August 2014.

[13] M. Johanning, A. Braun, D. Eiteneuer, C. Paape, C. Balzer, W. Neuhauser, and C. Wunderlich. Resonance-enhanced isotope-selective photoionization of YbI for ion trap loading. *Applied Physics B*, 103(2):327–338, May 2011.

[14] Thomas Lauprêtre, Lucas Groult, Bachir Achi, Michael Petersen, Yann Kersalé, Marion Delehaye, and Clément Lacroûte. Absolute frequency measurements of the $^1S_0 \rightarrow {}^1P_1$ transition in ytterbium. *OSA Continuum*, 3(1):50–57, January 2020. Publisher: Optica Publishing Group.

[15] Yaoxing Wu, Girik Jain, Tatyana Sizyuk, Xinbing Wang, and Ahmed Hassanein. Dynamics of laser produced plasma from foam targets for future nanolithography devices and X-ray sources. *Scientific Reports*, 11:13677, July 2021.

[16] Ming Cao, Jianjun Cao, Mian Liu, Yuan Sun, Meng Wu, Shiming Guo, and Shumei Gao. Wavelength dependence of nanosecond laser induced surface damage in fused silica from 260 to 1550 nm. *Journal of Applied Physics*, 123(13):135105, April 2018.

[17] Ryan J McGuigan and Helmut Kessler. Thermal laser induced damage in optical coatings due to an incident pulse train. *Proc. SPIE*, 11910:18, November 2021. Laser-Induced Damage in Optical Materials 2021.

[18] D.W. Fradin and Michael Bass. Comparison of laser-induced surface and bulk damage. *Applied Physics Letters*, 22(4):157–159, February 1973.

[19] Laurent Michaille, David Taylor, Charlotte Bennett, Terence Shepherd, Christian Jacobsen, and Theis Hansen. Damage threshold and bending properties of photonic

crystal and photonic band-gap optical fibres. *Proceedings of SPIE - The International Society for Optical Engineering*, 5618, November 2004.

[20] L. Torrisi, L. Andò, S. Gammino, J. Kràsa, and L. Làska. Ion and neutral emission from pulsed laser irradiation of metals. *Nuclear Instruments and Methods in Physics Research Section B: Beam Interactions with Materials and Atoms*, 184(3):327–336, 2001.

[21] Xiaohua Wang, Shudi Zhang, Xiaoling Cheng, Eryi Zhu, Wei Hang, and Benli Huang. Ion kinetic energy distributions in laser-induced plasma. *Spectrochimica Acta Part B: Atomic Spectroscopy*, 99:101–114, September 2014.

[22] J. I. Cirac and P. Zoller. Quantum Computations with Cold Trapped Ions. *Physical Review Letters*, 74(20):4091–4094, May 1995.

[23] M Sankari and M V Suryanarayana. Studies on the isotope selective photoionization of the low-abundant isotope. *Journal of Physics B: Atomic, Molecular and Optical Physics*, 31(2):261–273, January 1998.

[24] L. Torrisi, S. Gammino, L. Andò, and L. Làska. Tantalum ions produced by 1064 nm pulsed laser irradiation. *Journal of Applied Physics*, 91(7):4685–4692, March 2002.

[25] Roger Kelly. Gas dynamics of the pulsed emission of a perfect gas with applications to laser sputtering and to nozzle expansion. *Physical Review A*, 46(2):860–874, July 1992. Publisher: American Physical Society.